编号：SCIE-CY- 20250910-12

检索报告

根据委托人吴欣桐的委托，通过网络检索，吴欣桐发表的 2 篇论文被《科学引文索引》扩展版（SCI-Expanded）数据库收录。数据库具体检索结果如下：

1.标题：Microgalvanic cell-mediated green synthesis of Cu2O nanocubes with (100) facets for boosting dopamine hydrochloride sensing performance

作者：Ma, YY(Ma, Yiyue)[1]; Wu, XT(Wu, Xintong)[1]; Pan, HY(Pan, Haoyu)[1]; Zhu, WX(Zhu, Wenxin)[1]; Lu, CY(Lu, Chengyi)[2]; Wang, JL(Wang, Jianlong)[1]

期刊：TALANTA 卷：282 文献号: 126995

DOI: 10.1016/j.talanta.2024.126995

出版年: JAN 1 2025

在线发表时间:OCT 2024

已索引:2024-10-27

通讯作者地址: [Zhu, Wenxin; Wang, Jianlong] (corresponding author), Northwest A&F Univ, Coll Food Sci & Engn, 22 Xinong Rd, Yangling 712100, Shaanxi, Peoples R China

[Lu, Chengyi] (corresponding author), Northwestern Polytech Univ, Sch Marine Sci & Technol, Xian 710072, Peoples R China

地址:

1. Northwest A&F Univ, Coll Food Sci & Engn, 22 Xinong Rd, Yangling 712100, Shaanxi, Peoples R China
2. Northwestern Polytech Univ, Sch Marine Sci & Technol, Xian 710072, Peoples R China

出版商：ELSEVIER

Web of Science 类别: Chemistry, Analytical

文献类型: Article

语种：English

ISSN: 0039-9140

eISSN: 1873-3573

入藏号: WOS:001338648200001

Web of Science 核心合集中的 "被引频次"：1

第二作者吴欣桐，第一署名单位西北农林科技大学食品科学与工程学院。

通讯作者朱文新，王建龙，署名单位西北农林科技大学食品科学与工程学院。

通讯作者卢丞一，署名单位西北工业大学。

2025 年公布的影响因子: 6.1，JCR 分区情况：

JCR® 类别	*类别中的排序*	*JCR 分区*
CHEMISTRY, ANALYTICAL	**14/111**	**Q1**

2025 年公布的中科院分区（升级版）：

	学科名称	分区	Top 期刊
大类	化学	2	是
小类	CHEMISTRY, ANALYTICAL 分析化学	2	-

2.标题：Multipurpose biosensing electronics enabled by ultrasoft and durable hydrogel via ions pre-incorporation
作者：Ma, YY(Ma, Yiyue)[1]; Shang, CD(Shang, Congdi)[1]; Xu, YT(Xu, Yiting)[1]; Wu, XT(Wu, Xintong)[1]; Zhu, WX(Zhu, Wenxin)[3]; Tang, WZ(Tang, Wenzhi)[1]; Tan, H(Tan, Hai)[2]; Wang, JL(Wang, Jianlong)[1]
期刊：ADVANCED COMPOSITES AND HYBRID MATERIALS 卷：8 期：5 文献号: 342
DOI: 10.1007/s42114-025-01422-x
出版年: AUG 28 2025
已索引:2025-08-31
通讯作者地址: [Tang, Wenzhi; Wang, Jianlong] (corresponding author), Northwest A&F Univ, Coll Food Sci & Engn, 22 Xinong Rd, Yangling 712100, Shaanxi, Peoples R China
[Tan, Hai] (corresponding author), Northwest A&F Univ, Coll Mech & Elect Engn, 22 Xinong Rd, Yangling 712100, Shaanxi, Peoples R China
地址:
1. Northwest A&F Univ, Coll Food Sci & Engn, 22 Xinong Rd, Yangling 712100, Shaanxi, Peoples R China
2. Northwest A&F Univ, Coll Mech & Elect Engn, 22 Xinong Rd, Yangling 712100, Shaanxi, Peoples R China
3. Peking Univ, Sch Mat Sci & Engn, Beijing 100871, Peoples R China
出版商：SPRINGERNATURE
Web of Science 类别: Nanoscience & Nanotechnology ;Materials Science, Composites
文献类型: Article
语种：English
ISSN: 2522-0128
eISSN: 2522-0136
入藏号: WOS:001559087300001
Web of Science 核心合集中的 "被引频次"：0
第四作者吴欣桐，第一署名单位西北农林科技大学食品科学与工程学院。
通讯作者唐文志，王建龙，署名单位西北农林科技大学食品科学与工程学院。
通讯作者谭海，署名单位西北农林科技大学机械与电子工程学院。

2025 年公布的影响因子: 21.8，JCR 分区情况：

JCR® 类别	*类别中的排序*	*JCR 分区*
MATERIALS SCIENCE, COMPOSITES	**1/34**	**Q1**
NANOSCIENCE & NANOTECHNOLOGY	**7/147**	**Q1**

2025 年公布的中科院分区（升级版）：

	学科名称	分区	Top 期刊
大类	材料科学	1	是
小类	MATERIALS SCIENCE, COMPOSITES 材料科学：复合	1	-
小类	NANOSCIENCE & NANOTECHNOLOGY 纳米科技	1	-

查证检索：

西北农林科技大学图书馆
2025 年 9 月 10 日

西北农林科技大学
NORTHWEST A&F UNIVERSITY

荣誉证书

HONORARY CREDENTIAL

该团队在2023年寒假优秀学子回访母校社会实践活动中，表现突出，被评为“优秀团队”，特发此证，以资鼓励。

队长：路天一

队员：吴欣桐 张哲菲

西北农林科技大学招生办公室

2023年4月

CULSC第十届全国大学生生命科学竞赛（创新创业类）

获奖证书

获奖项目： 基于微原电池介导的具有（100）晶面的氧化亚铜（Cu_2O）纳米立方体的绿色合成及其对提升盐酸多巴胺电化学传感性能的研究

获奖学生： 吴欣桐 吴彦霖 李灿 李佳颖 李昀晏

指导老师： 王建龙

获奖单位： 西北农林科技大学

获奖类型： 二等奖

证书编号： CULSC2025CE0797

全国大学生生命科学竞赛委员会

二〇二五年七月

西北农林科技大学
NORTHWEST A&F UNIVERSITY

大学生创新创业训练计划项目

结题证书

吴欣桐同学主持，徐依婷、潘皓瑜同学参与的校级项目“整体式铜基催化剂用于猪饲料中盐酸多巴胺电化学传感”（No.X202410712585）顺利结题，评审结果为优秀，指导教师为朱文新，特此证明。

西北农林科技大学

教务处

二零二五年五月二十八日

Talanta 282 (2025) 126995

Contents lists available at ScienceDirect

Talanta

journal homepage: www.elsevier.com/locate/talanta

Microgalvanic cell-mediated green synthesis of Cu_2O nanocubes with (100) facets for boosting dopamine hydrochloride sensing performance

Yiyue Ma [a], Xintong Wu [a], Haoyu Pan [a], Wenxin Zhu [a,**], Chengyi Lu [b,***], Jianlong Wang [a,*]

[a] College of Food Science and Engineering, Northwest A&F University, 22 Xinong Road, Yangling, 712100, Shaanxi, China
[b] School of Marine Science and Technology, Northwestern Polytechnical University, Xi'an, 710072, China

ARTICLE INFO

Keywords:
Cu_2O nanocubes
Low-index facets
Electrochemical sensor
Facet-dependent sensing

ABSTRACT

Despite numerous efforts have been made on exploring the preparation, properties and application of Cu_2O nanocrystal, there is still a lack of a facile and green synthesis strategy to obtain well-defined Cu_2O nanocubes (NCs). And exploration of the superior low-index lattice plane of Cu_2O in electrochemical sensing is also inadequate. Herein, we proposed a $Ni(OH)_2$-mediated in-situ synthetic strategy for the preparation of Cu_2O NCs enclosed by low-index facets with simple procedure, mild temperature and low energy-consumption. The $Ni(OH)_2$ sites not only facilitated the contact between Cu^{2+} and the substrate Ni foam (NF), but also can combine with the NF to act as a primary battery to regulate the nucleation and growth rate of Cu_2O (100) facets. Benefiting from the high ratio of exposed electroneutral (100) lattice planes of nanocubes, the Cu_2O NCs formed on $Ni(OH)_2$-abundant Ni Foam (Cu_2O NCs/NF_{EO}) exhibited a wide linear range (3.25–1178.8 μM), a low detection limit (1.86 μM) and a high sensitivity (900 μA mM^{-1} cm^{-2}) in dopamine hydrochloride (DAH) electrochemical sensing. This work expects to provide more clues about the relationship between different dominant low-index facets of Cu_2O NCs and electrochemical sensing performance towards DAH, and thereby contributes to the development of functional materials based on Cu_2O nanocrystals with desirable facets.

1. Introduction

Metal oxides nanomaterials (NPs) offer practical and promising solutions to realize outstanding performance in various applications on account of their unique and exciting properties [1]. Among those metal oxides, Cu_2O nanomaterials have attracted growing interest in the area like catalysis (electrocatalysis, photocatalysis and organocatalysis) and sensing (electrochemical sensing, surface-enhanced Raman sensing and photoelectricity sensing) due to their non-toxic, inexpensive and easily-available properties [2–5]. Thereinto, widespread attention has been paid to the development and investigation of Cu_2O nanocrystals which possess sufficient redox capacity, varied morphology and unique properties like facet-dependent property [6]. Cu_2O nanocrystals present a cubic structure, in which the tetrahedron of Cu atoms are surrounded by O atoms while every Cu atom corresponds to two neighboring O atoms in the model of unit cell [7]. The special electrical properties of Cu_2O nanocrystal render it considerable potential to be applied for various electrochemical reactions with favorable activity and selectivity. Hence substantial numbers of attempts have been made to create diverse variety of engineered Cu_2O nanocrystals for the construction of high-efficiency electrochemical sensors with accurate sensing signal.

At present, diverse Cu_2O nanostructures have been reported as promising candidate materials in catalysis and sensing, such as cubes, octahedra, cuboctahedra, rhombic dodecahedral crystals and nanowires [8]. Among the various types of Cu_2O nanocrystals, the cubic and octahedral structures occupy an important position because of their preferable capacity to be converted into other structural forms [9]. To obtain Cu_2O nanocrystals with desired physical and chemical properties, a universal strategy is to tune the exposed facets to acquire requisite surface energies and electronic structures [6]. And Cu_2O nanocrystals enclosed by low-index planes have attracted broader concern owing to their good controllability, simple synthetic route and low energy consumption in preparation as well as favorable stability in catalysis and sensing [10]. The basic Cu_2O crystals composed of low-index facets can be divided in different types that are enclosed by the (100), (111), and (110) facets, respectively [10,11]. In the quest to prepare Cu_2O

* Corresponding author.
** Corresponding author.
*** Corresponding author.
E-mail addresses: zhuwx@nwafu.edu.cn (W. Zhu), luchengyi@nwpu.edu.cn (C. Lu), wanglong79@nwsuaf.edu.cn (J. Wang).

https://doi.org/10.1016/j.talanta.2024.126995
Received 13 August 2024; Received in revised form 11 September 2024; Accepted 3 October 2024
Available online 10 October 2024

nanocrystals with well-defined morphology and specific facets, the primarily applied tactic is solution phase synthesis, in which the nucleation and growth behaviors of Cu_2O crystals can be well controlled and thus nanocrystals with required exposed facets can be obtained [7]. In general, for solution phase synthesis, $Cu(OH)_2$ precursor firstly forms through the combination of Cu^{2+} and OH^- in alkaline conditions, and then the Cu_2O nanocrystals are obtained from the conversion of $Cu(OH)_2$ under the action of reductants like NH_2OH, ascorbic acid and sodium citrate [12–14]. Whereas, it should be noted that in order to precisely acquire the nanocrystals with certain exposed lattice planes, most of the related researches either highly rely on the utilization of capping agent or require relative strict control of reaction conditions like pH and temperature [8,15]. And a facile and green synthetic pathway to prepare the Cu_2O nanocrystals with well-defined morphology is still highly demanded.

Furthermore, although there are numerous studies that have reported the success preparation of Cu_2O-based electrochemical sensors and their excellent performance in practical application, the unique sensing mechanism of Cu_2O nanocubes enclosed with low-index lattice planes have not been fully explored. In this work, we proposed an in-situ synthetic strategy mediated by microgalvanic cells for the formation of Cu_2O nanocubes with well-defined facets on Ni Foam substrate (Cu_2O NCs/NF_{EO}), which was free from the dependence on the addition of alkaline substances, capping agents or reductants. Then an electrochemical sensor based on the Cu_2O NCs/NF_{EO} was developed for the determination of dopamine hydrochloride (DAH), which exhibited a wide linear range (3.25–1178.8 μM), a low detection limit (1.86 μM) and a high sensitivity (900 μA mM^{-1} cm^{-2}) in sensing. The designed electrochemical DAH sensor offers an economic and efficient way for the accurate determination of DAH, which also exhibits promising potential to be applied in portable sensor and wearable sensor. Moreover, to gain the insights into the superior low-index lattice planes of Cu_2O NCs/NF_{EO} in electrochemical sensing towards DAH, we conducted the corresponding density functional theory (DFT) calculations to explore the adsorption between DAH molecules and different exposed low-index facets of Cu_2O. This work aims to evaluate the utilization potentiality of Cu_2O nanocubes enclosed with different low-index facets in electrochemical sensing and clarify the corresponding sensing mechanism to provide valuable inspiration for further development of electrochemical sensors based on Cu_2O nanocrystals.

2. Results and discussion

2.1. Characterization

As illustrated in Fig. 1, this work tactfully utilized the partly oxidized Ni foam (NF_{EO}) with $Ni(OH)_2$ sites to construct a quantity of micro-primary cell for the synthesis of Cu_2O nanocubes (NCs) with low-index (100) facets. And the electrochemical sensor based on Cu_2O NCs/NF_{EO} exhibited superior sensing performance like depressed oxidation potential and elevated response current in DAH detection. Compared with conventional method, the proposed strategy liberates the production of Cu_2O NCs from the high energy consumption and the dependence on the use of reagent like alkali, capping agents and reductants, providing a facile and green route for the preparation of Cu_2O NCs-based electrodes.

The morphology was characterized by Scanning electron microscope (SEM). As shown in Fig. 2a, we can clearly observe that the Cu_2O NCs uniformly formed on the skeletons of NF_{EO}. And with the prolongation of immersing time, the amount of Cu_2O NCs loaded on the surface of NF_{EO} is significantly increased (Fig. S1). The average size of the Cu_2O NCs on NF_{EO} was calculated to 260–350 nm according to the corresponding SEM images in Fig. 2a. Whereas, the Cu_2O synthesized on the NF_O depicted an irregular particulate appearance instead of cube-shaped structure (Fig. S2) and the Cu NPs synthesized on NF_E exhibited tiny particulate morphology accompanied with relative low loading, which can be ascribed to influence of different surface composition of substrate.

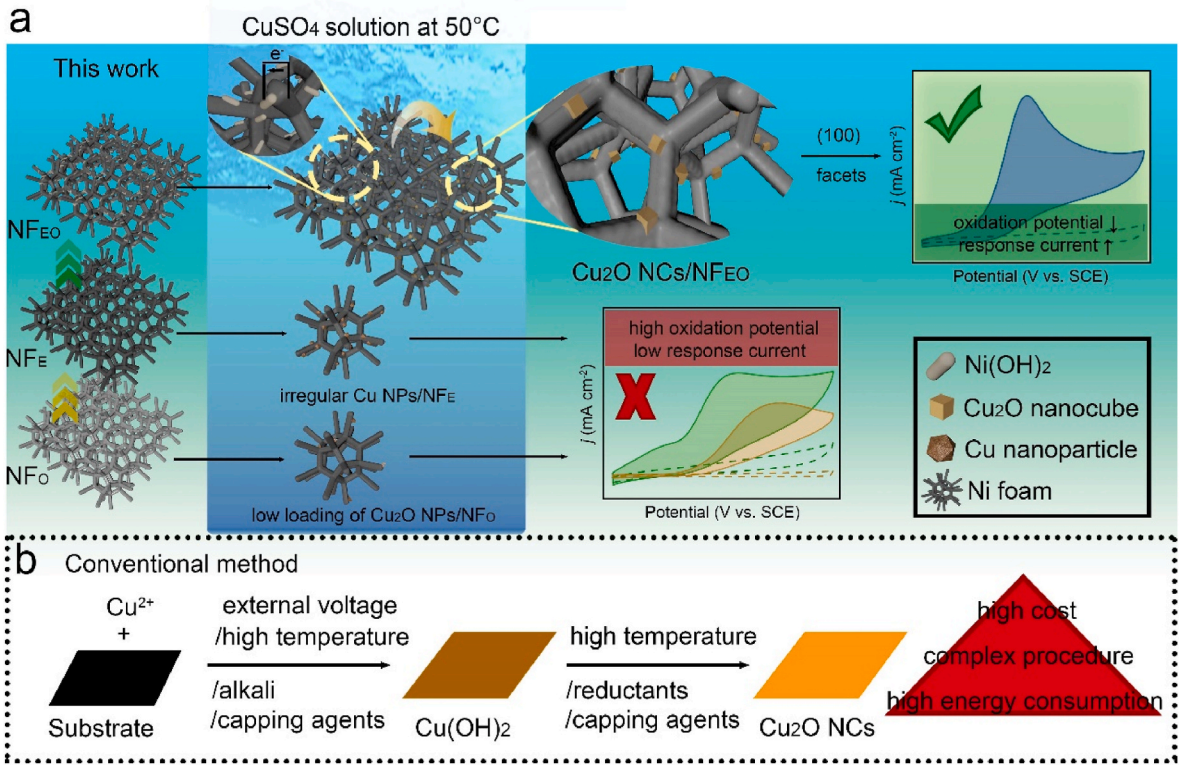

Fig. 1. Schematic illustration of (a) the synthesis process and the excellent sensing performance of Cu_2O NCs/NF_{EO} and the advantages of proposed $Ni(OH)_2$-mediated strategy over (b) conventional method.

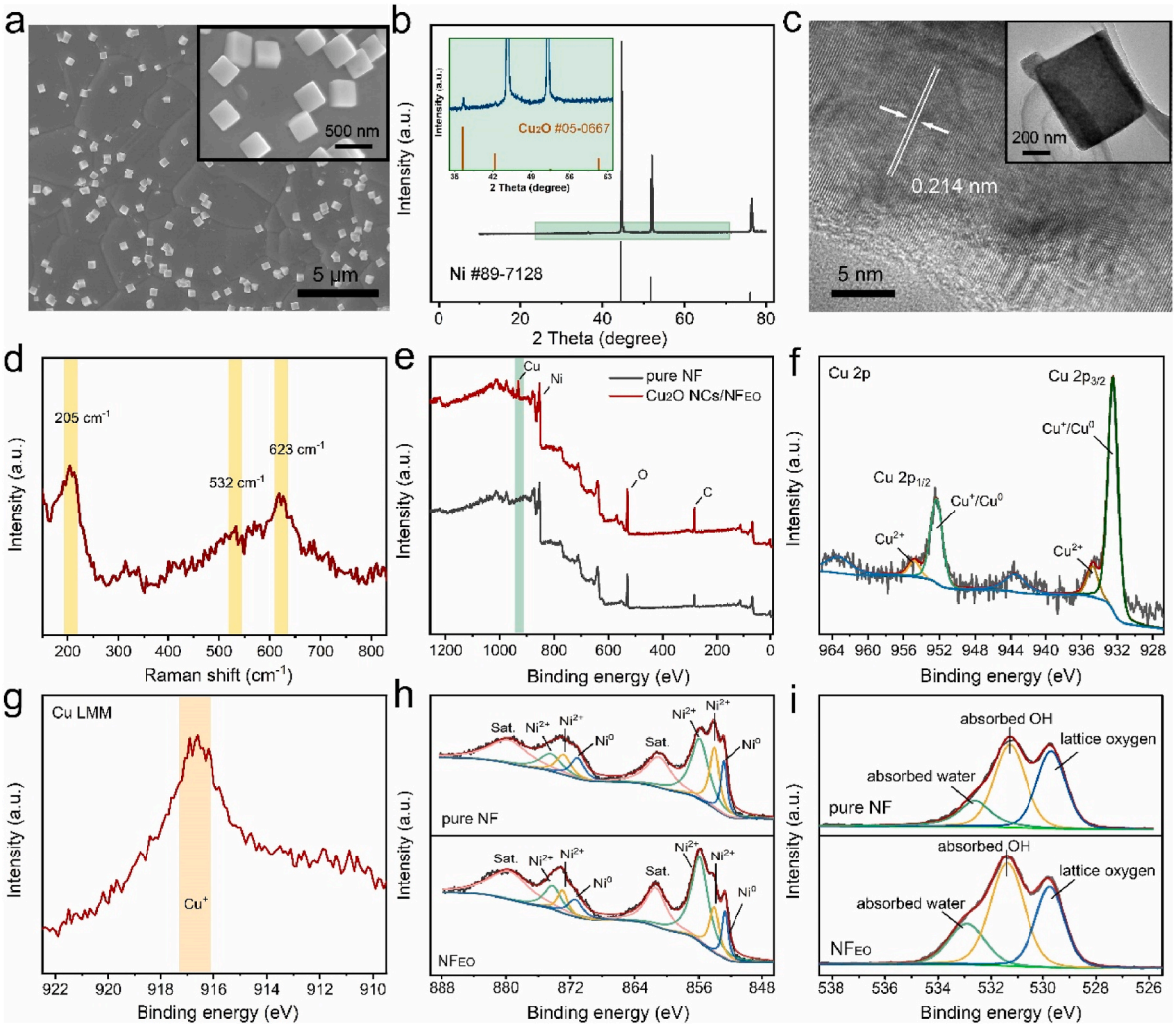

Fig. 2. (a) SEM image of Cu_2O NCs/NF_{EO} (Inset: partial enlarged view of Fig. 2a). (b) XRD pattern of Cu_2O NCs/NF_{EO} (Inset: partial enlarged view of Fig. 2b). (c) The lattice fringes of Cu_2O NCs/NF_{EO} in TEM image (Insert: HRTEM image of Cu_2O NCs). (d) Raman spectrum of Cu_2O NCs/NF_{EO}. (e) XPS survey spectra of pure NF and Cu_2O NCs/NF_{EO}. (f) XPS Cu 2p spectrum of Cu_2O NCs/NF_{EO}. (g) Cu LMM Auger spectrum of Cu_2O NCs/NF_{EO}. (h) XPS Ni 2p spectra of pure NF and NF_{EO}. (i) XPS O 1s spectra of pure NF and NF_{EO}.

X-ray diffraction (XRD) was utilized to investigate the formation of Cu_2O particles. X-ray diffraction (XRD) pattern of Cu_2O NCs was given in Fig. 2b, in which the peaks at 44.8°, 52.0° and 76.5° can be indexed to Ni foam (JCPDS 89–7128) and the peaks at 36.6°, 42.4° and 61.4° can be indexed to the (111), (200) and (220) diffraction peaks of Cu_2O (JCPDS 05–0667). Although the overall peak intensity of Ni foam is much higher than Cu_2O, the sharp peaks of Cu_2O crystals still can be observed, indicating their good crystallinity. And the intensity ratio between the (111) and (200) peaks of Cu_2O was calculated to be 1.88, which is lower than the reference value (2.7) of standard powder, indicating the abundant (100) facets of the Cu_2O nanocubes prepared on NF_{EO} [16]. It should be noted when the substrates were changed from to NF_{EO} to NF_E and NF_O, the obtained electrodes didn't show the diffraction peaks of Cu_2O in their XRD patterns (Fig. S3a) despite the signal of Cu^+ can be observed in Cu_2O NPs/NF_O (Figs. S3b–c), which suggested that the formation of Cu_2O NCs was strongly dependent on the substrate. The TEM images of Cu_2O NCs synthesized on NF_{EO} also exhibited a typical cube structure (Fig. 2c). And the HRTEM present lattice distance of 0.213 nm, corresponding to the Cu_2O (200) plane.

Then Raman spectroscopy was also utilized to characterize the composition of Cu_2O NCs materials. As illustrated in Fig. 2d, the three binding energy peaks at 205, 532 and 623 cm^{-1} could be attributed to the characteristic Raman bands of Cu_2O, while another two peaks located at ~330 and 571 cm^{-1} could be assigned to the CuO phase generated due to sample drying and sample storage [17,18]. These above results revealed the success preparation of Cu_2O NCs/NF_{EO} with low-index lattice planes.

In order to further investigate the element composition of Cu_2O NCs/NF_{EO}, the X-ray photoelectron spectroscopy (XPS) measurements were carried out and the results were given in Fig. 2e–g. The XPS survey spectra of Cu_2O NCs/NF_{EO} in Fig. 2e revealed the existence of Cu, Ni, O and C elements, confirming the success introduction of Cu element on the surface of NF_{EO} after being immersed in $CuSO_4$ solution. Then the further analysis of valence state was conducted through collecting high-resolution XPS spectra of Cu element. As shown in Fig. 2f, the two high peaks at ~932.5 and ~952.3 eV can be respectively ascribed to the Cu $2p_{3/2}$ and Cu $2p_{1/2}$ of Cu^+/Cu^0, while the other two peaks related to Cu^{2+} can also be observed at ~934.7 and ~954.8 eV, which can be attributed to the partial oxidation of Cu_2O NCs on the surface occurred in sample drying and sample storage. Another two peaks at ~963.3 and ~943.5 eV were the satellite peaks. As the binding energy of Cu^+ and Cu^0 is very close to each other (0.1 eV), it's usually difficult to distinguish their signals in the core-level Cu 2p spectrum. Thus, we collected the auger spectra of Cu LMM signal of Cu_2O NCs/NF_{EO} (Fig. 2g), and only the typical peak of Cu^+ located at 916.6 eV could be observed, suggesting the success synthesis of Cu_2O NCs.

Besides, in consideration of the fact that Cu_2O NCs with well-defined cubic morphology and low-index lattice planes can only be synthesized on the surface of NF_{EO}, we also investigated the XPS spectra of NF_{EO} and pure NF to figure out the difference between them to ascertain the key factor for the preparation of Cu_2O NCs/NF_{EO}. The high-resolution XPS spectra of Ni element were collected to compare the valence state of Ni element in NF_{EO} and pure NF. As shown in Fig. 2h, the XPS spectra of pure NF exhibited two shake-up satellite peaks at 879.6 and 861.0 eV. Additionally, the two distinct peaks centered at 874.4 and 855.9 eV can match well with the Ni $2p_{3/2}$ and Ni $2p_{1/2}$ of $Ni(OH)_2$, respectively [19,20]. And the two peaks at 872.8 and 854.1 eV corresponded to the Ni $2p_{3/2}$ and Ni $2p_{1/2}$ of Ni^{2+}, respectively [19,20]. In addition, the peaks located at 871.1 and 852.9 eV can be attributed to Ni^0 [21]. The Ni 2p spectrum of NF_{EO} can also be deconvoluted to the peaks related to Ni $(OH)_2$, Ni^{2+} and Ni^0 while the ratio of valence state of Ni element varied compared with pure NF. After etching treatment, the NiO layer caused by the surface oxidation was partly removed while more $Ni(OH)_2$ active sites are efficiently exposed, which can also be confirmed by the obvious increase of absorbed OH in the O 1 s XPS spectrum of NF_{EO}. As shown in Fig. 2i, the three prominent peaks centered at ~529.7, ~531.3 and ~532.6 eV can be assigned to the absorbed water, absorbed OH and lattice oxygen, respectively [22,23]. And it should be noted that the proportion of $Ni(OH)_2$ reduced after the growth of Cu_2O nanocrystals, which suggested that the $Ni(OH)_2$ on the surface of NF_{EO} might act as seed sites to mediate the formation of Cu_2O nanocubes with low-index lattice planes (Fig. S4, Table S1). Besides, from the XPS survey spectra of NF_{EO} and pure NF in Fig. S5, it can be observed that apart from the intrinsic elements like C, O and Ni of pure NF, an extra Cl element emerged in the XPS survey spectra of NF_{EO}, which can be attributed to the residual HCl in the etching of NF.

Based on the above analysis, one of the important reasons for the success synthesis of Cu_2O NCs on NF_{EO} can be attributed to the improvement of wetting ability and the introduction of Cl^- during etching process. The enhanced wetting ability makes the Cu^{2+} ions easy to access and participant in synthetic reaction and the residual Cl^- assists the formation of cubic Cu_2O particles [1,24]. Thus, both of the Cu_2O NCs/NF_{EO} and Cu NPs/NF_E showed higher loadings and more distinct granular appearance than Cu_2O NPs/NF_O, as shown in Fig. 2a and Fig. S2. However, although the Cl^- introduced in etching can enhance the adsorption of Cu^{2+} and influence the nucleation and growth rate, most of the Cu_2O NPs on NF_E are irregular particles instead of well-defined nanocubes, which can be ascribed to the influence of omission of oxidation process after etching treatment. Specifically, the surface OH formed in oxidation can facilitate the connection between the water molecule and the substrate material, and the $Ni(OH)_2$ on the NF_{EO} could mediate the formation of Cu_2O nanocubes through the formation of plenty of micro-primary battery, based on which the Cu^{2+} adsorbed on the surface of substrate and in-situ converted into Cu_2O nanocubes with low-index (100) facets.

2.2. Electrochemical sensing performance of electrode

To investigate the electron transfer resistance of prepared electrodes, electrochemical impedance spectroscopy (EIS) was measured in 5 mM $[Fe(CN)_6]^{3/4-}$ containing 0.1 M KCl (Fig. 3a). The smaller semicircle in the Nyquist plot of Cu_2O NCs/NF_{EO} indicated that the introduction of Cu_2O NCs can reduce the charge transfer resistance (R_{ct}) and facilitate the charge transport efficiency, which is closely related to the electrochemical activity of electrodes. And the electrochemical surface area (ECSA) of pure NF and Cu_2O NCs/NF_{EO} was estimated by recording the CV curves in 0.1 M PB with scan rates ranging from 10 to 100 mV s^{-1} (Fig. 3b, Fig. S6). The ECSA of Cu_2O NCs/NF_{EO} was calculated to be 0.42 mF cm^{-2}, showing a significant improvement compared with its precursor (pure NF, 0.05 mF cm^{-2}), which can efficiently enhance the electrochemical sensing signal of Cu_2O NCs/NF_{EO} in the detection of DAH.

The electrochemical oxidation capability was investigated by recording the CV curves of different electrodes in 0.1 M PB with and without 1 mM DAH (Fig. 3c–f). It can be seen that on the surface of Cu_2O NCs/NF_{EO} electrode, there is only irreversible electrochemical oxidation reaction for DAH, and the oxidation peak towards DAH appeared at 0.233 V with a peak current density of 2.02 mA cm^{-2}. Compared with its

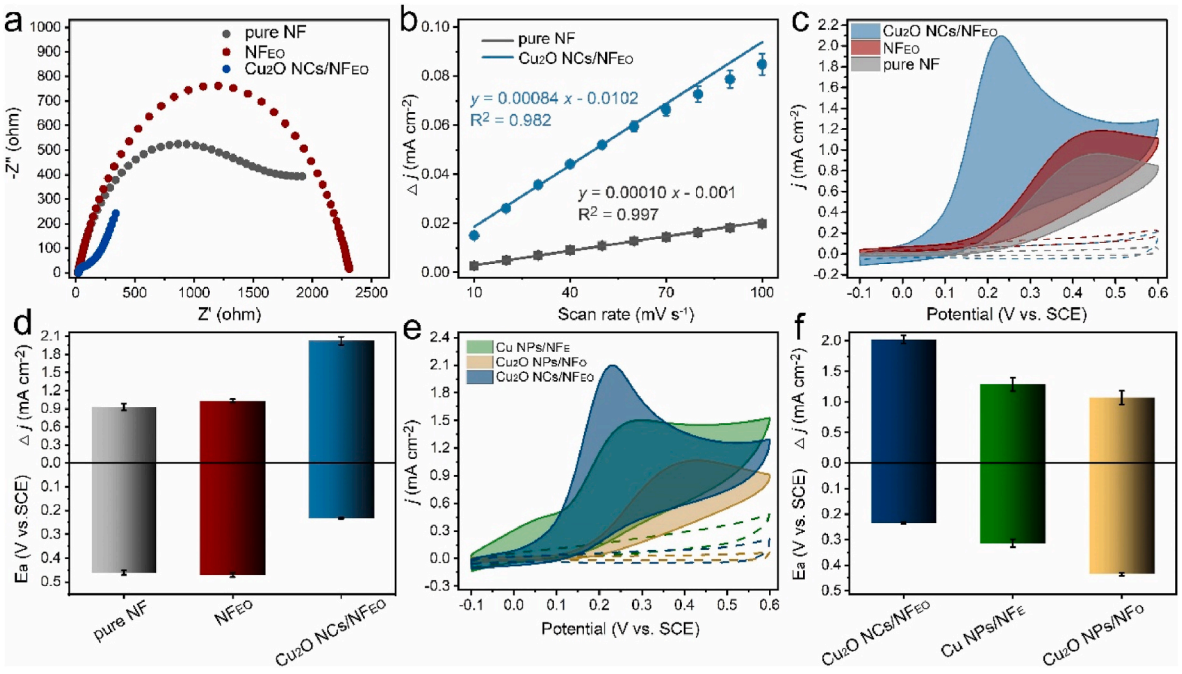

Fig. 3. (a) The Nyquist curves of pure NF, NF_{EO} and Cu_2O NCs/NF_{EO}, (b) The calculation of C_{dl} of NF (blue line) and Cu_2O NCs/NF_{EO} (gray line) in 0.1 M PB, (c) CV curves of NF (gray part), NF_{EO} (red part) and Cu_2O NCs/NF_{EO} (blue part) in 0.1 M PB with 1 mM DAH (solid line) and without DAH (dashed line) and (d) the corresponding column chart. (e) CV curves of Cu_2O NPs/NF_O (yellow part), Cu NPs/NF_E (green part) and Cu_2O NCs/NF_{EO} (blue part) in 0.1 M PB with 1 mM DAH (solid line) and without DAH (dashed line) and (f) the corresponding column chart.

precursors (pure NF and NF_{EO}), the proposed Cu_2O NCs/NF_{EO} electrode shows an improved oxidation peak current and lowest peak potential, indicating the high electrochemical oxidation capability induced by surface Cu_2O NCs, which is conducive to realizing better electrochemical sensing performance towards DAH. In addition, the CV curves of Cu_2O NPs/NF_O and Cu NPs/NF_E in the presence of 1 mM DAH were also measured to investigate the electrochemical oxidation capability of electrodes prepared on different substrates. It can be observed that compared with Cu_2O NCs/NF_{EO} electrodes, the Cu_2O NPs/NF_O electrodes and the Cu NPs/NF_E electrodes exhibit lower oxidation peak current towards the DAH. The Cu_2O NCs/NF_{EO} electrode showed a higher peak current of 2.02 mA cm^{-2} and a decreased anodic peak potential (E_a) of 0.23 V compared with those of Cu NPs/NF_E (1.29 mA cm^{-2}, 0.31 V) and Cu_2O NPs/NF_{EO} (1.07 mA cm^{-2}, 0.44 V), indicating the better electrochemical oxidation capability and the higher response signal of Cu_2O NCs/NF_{EO} with higher ratio of (100) facets.

The main reason for the superior electrochemical performance of Cu_2O NCs/NF_{EO} can be attributed to the distinct properties of (100) facets. Although some common advantages exist in all the low-index planes of Cu_2O like relative low surface energies and favorable stability, there are still difference between (111), (110) and (100) planes. Density functional theory, as a theory of electronic structure formulated in terms of the electron density as the basic unknown function, can provide insight into sensing mechanisms at atomic scale. Therefore, DFT calculation was conducted to calculate the DAH adsorption energy on the surface of Cu_2O with different facets and figure out the difference of the affinity between DAH molecules and different types of low-index facet edges. DAH molecule was firstly adsorbed on the surface of different crystal edges and the lengths of formed Cu–O bonds were measured as 1.91 Å for (100) plane, 2.07 Å for (110) plane, and 2.65 Å for (111) plane. As shown in Fig. 4, the (100) plane also exhibited the lowest adsorption energy of −1.64 eV compared with (111) plane (−0.05 eV) and (110) plane (1.98 eV). The shortest bond length and the highest negative binding energy between Cu_2O (100) facet and DAH implied the stronger affinity of (100) crystal edge to DAH molecules among the exposed low-index facets that we investigated, which is conducive to realize superior response signal and high sensitivity in DAH electrochemical sensing. And the higher affinity of (100) plane can also be ascribed to the electrostatic interaction. Owing to the different under-coordinated Cu atoms induced by varied atomic arrangements, the (100) facet terminated by O atoms displayed electric neutrality instead of the electropositive properties of the (111) and (110) planes due to the dangling Cu atoms [6]. During the testing process, the DAH molecules are positively charged owing to the weak alkaline environment provided by PB solution (pH = 7.5), which conduces to the better combination between DAH and the surface of (100) planes because of the reduced electrostatic repulsion. And the order of charged property of Cu_2O are in the following order: (100) < (111) (positively charged) < (110) (positively charged), which is consistent with the results in DFT calculations. Thus, the significantly increased oxidation peak current of Cu_2O NCs/NF_{EO} electrode can be attributed to their high ratio of exposed electroneutrality (100) facets and the resulting stronger affinity with DAH molecules.

Besides, the electrochemical behavior of Cu_2O NCs/NF_{EO} electrode in the existence of DAH was also studied. Fig. S7 shows the CV curves of Cu_2O NCs/NF_{EO} electrode in 1 mM DAH at different scan rates (10–100 mV s^{-1}). It can be observed in Fig. 5a that there is a good linear relationship between the current density of oxidation peak and the square root of scan rates, which is calculated to be $\triangle j$ (mA cm^{-2}) = 0.323 v ($mV^{1/2}$ $s^{-1/2}$) - 0.230, with a correlation coefficient (R^2) of 0.987, indicating a surface diffusion-controlled process of DAH on the Cu_2O NCs/NF_{EO} electrode.

The pH values of electrolyte solutions have a considerable influence on the electrochemical behavior of DAH. Thus, we collected the CV curves of Cu_2O NCs/NF_{EO} electrode in the presence of 1 mM DAH in 0.1 M PB under different pH values. As shown in Fig. 5b and c, with the pH values ranging from 6.0 to 7.5, the position of oxidation peak shifted negatively while its current density gradually increased and reached the highest values at pH of 7.5. And when pH values exceeded 8.0, the peak current declined, which might be related to electrostatic effect between positively charged DAH molecules and electroneutrality (100) facets. Therein, 7.5 was considered as the optimum pH value of electrolyte, which was applied in subsequent experiments. And the CV curves of Cu_2O NCs/NF_{EO} electrode prepared under different synthetic temperature, synthetic time and different cupric salt used for immersion were also recorded to obtain the optimum parameters for the synthesis of

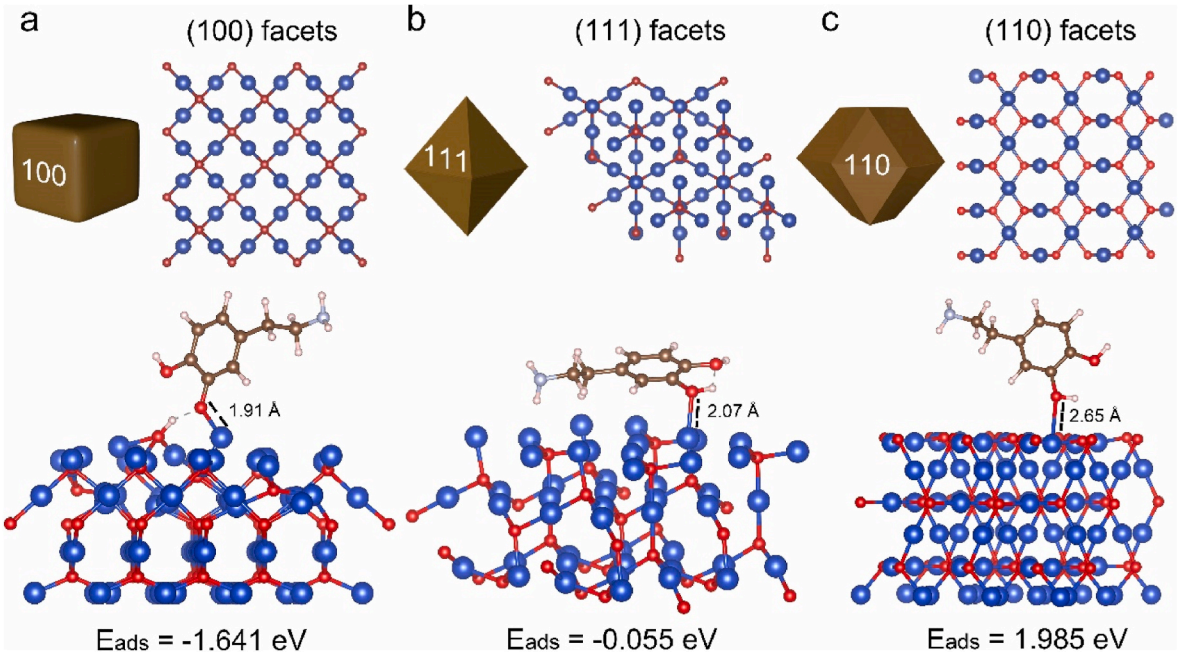

Fig. 4. Illustration of the structure of (100), (111), and (110) facet of Cu_2O and the optimized structures of DAH molecules adsorbed on the surface of Cu_2O (100), Cu_2O (111), and Cu_2O (110).

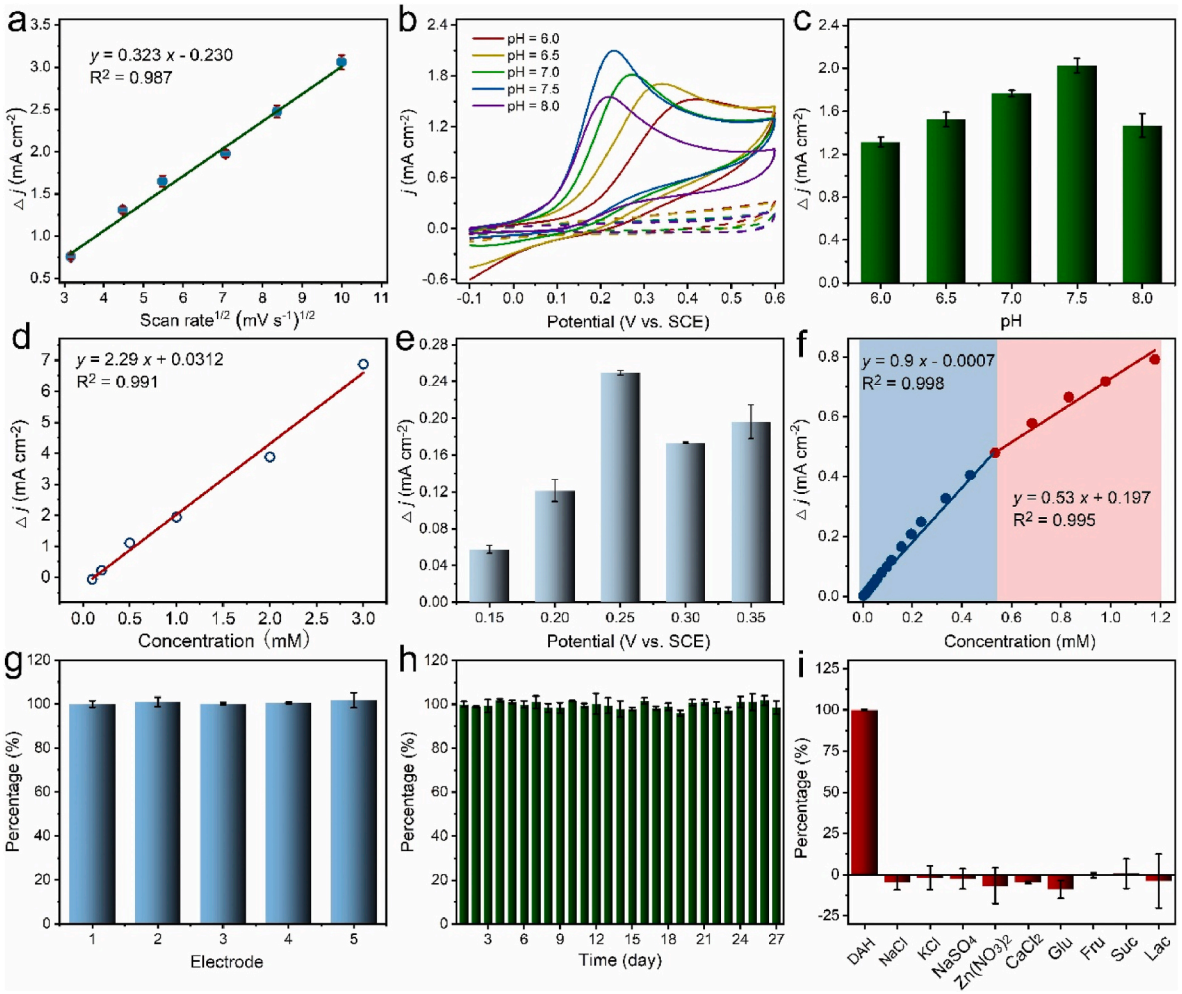

Fig. 5. (a) The fitted curve of the current density in CV curves of Cu_2O NCs/NF_{EO} recorded in 1 mM DAH at different scan rates (10–100 mV s^{-1}). (b) The CV curves of Cu_2O NCs/NF_{EO} collected in different pH values (solid line: CV curves recorded in the presence of 1 mM DAH, dashed line: CV curves recorded in 0.1 M PB) and (c) The corresponding column chart of peak current density. (d) The fitted curve of the current density in CV curves of Cu_2O NCs/NF_{EO} collected in different concentrations of DAH (0.1–3 mM). (e) The cartogram of the peak current density in amperometric curves of Cu_2O NCs/NF_{EO} under different potential (0.15–0.35 V). (f) The working curves of Cu_2O NCs/NF_{EO} obtained by amperometric measurement. (g) The reproducibility of five dependently prepared Cu_2O NCs/NF_{EO} electrodes. (h) The stability of Cu_2O NCs/NF_{EO} electrodes stored for 1–27 days. (i) Selectivity of Cu_2O NCs/NF_{EO} electrodes with the addition of DAH and interfering substances.

materials. Based on the results in Fig. S8, the Cu_2O NCs/NF_{EO} electrode was prepared through immersing the NF_{EO} in $CuSO_4$ solution for 30 min under 50 °C and applied for subsequently experiments.

Fig. S9 exhibits CVs of the Cu_2O NCs/NF_{EO} electrode with the addition of different concentrations of DAH. The oxidation peak current increased accompanied with the increase of DAH concentration. And the corresponding linear relationship is calculated to be $\triangle$j (mA cm^{-2}) = 2.29 C (mM) + 0.0312, with a correlation coefficient (R^2) of 0.991 (Fig. 5d). The good linear relationship suggested the potential of Cu_2O NCs/NF_{EO} electrode to be utilized for the quantitative determination of DAH.

Amperometry, as a more sensitive technique, was used for further evaluation of electrochemical sensing performance of Cu_2O NCs/NF_{EO}. To determine the optimum potential applied in amperometric measurement, we tested the response current of Cu_2O NCs/NF_{EO} under different potentials ranging from 0.15 V to 0.35 V with the addition of 25 μM DAH (Fig. 5e). And the maximum response current appeared at the potential of 0.25 V, which was applied in subsequent amperometric measurement as the optimum potential. The sensing performance of prepared electrodes was also studied through amperometric response test. As shown in Fig. S10, with the addition of 25 μM DAH, Cu_2O NCs/NF_{EO} exhibited approximately 2.6 times higher response current compared to that of pure NF. And the enhanced response signal can be attributed to the larger electrochemically active surface area, excellent oxidation capability and improved analyte-capturing ability of the Cu_2O NCs/NF_{EO} electrode.

The electrochemical sensing performance of Cu_2O NCs/NF_{EO} electrode was investigated by amperometric method under the optimum experimental conditions (Fig. 5f, Fig. S11). With the addition of different concentrations of DAH, the response current exhibited two-stage linearly increase following two linear equations as $\triangle j$ (mA cm^{-2}) = 0.9 C (mM) - 0.0007 (R^2 = 0.998) and $\triangle j$ (mA cm^{-2}) = 0.53 C (mM) + 0.197 (R^2 = 0.995). The proposed DAH electrochemical sensor based on Cu_2O NCs/NF_{EO} electrode showed a sensitivity of 900 μA mM^{-1} cm^{-2} with the concentration ranging from 3.25 μM to 533.8 μM and another sensitivity of 530 μA mM^{-1} cm^{-2} in the concentration range of 533.8 μM–1178.8 μM. And the corresponding detection limit was calculated to be 1.86 μM (S/N = 3). As shown in Table S2, compared with those previously reported electrochemical DAH sensor composed of metal oxides, the developed sensor based on Cu_2O NCs/NF_{EO} electrode displayed desirable sensing performance towards DAH, including a wider linear range, a higher sensitivity, a lower LOD values and a shorter response time. And the main reason for its superior electrochemical performance can be stated as follows. The $Ni(OH)_2$-mediated synthesis of Cu_2O NCs/NF_{EO} not only contributed to the uniform dispersion of nanocrystals and the formation of well-defined nanocubes composed of stable low-index

planes, but also raised the ratio of (100) planes in the Cu_2O nanocubes, thus leading to the reduced oxidation potential and improved electrocatalytic oxidation capacity towards DAH as well as the enhanced response current.

Reproducibility is an essential factor to be considered in ensuring the practicality of proposed sensor. Therein, we tested the CV curves of five independently prepared Cu_2O NCs/NF_{EO} electrodes in the presence of 1 mM DAH (Fig. 5g). And from the corresponding column chart, it can be seen that the oxidation peak current of different batches of Cu_2O NCs/NF_{EO} electrodes was close to each other, and the RSD value was calculated to be 1.41 %, indicating a satisfying reproducibility of Cu_2O NCs/NF_{EO} towards DAH sensing. In addition, the stability of sensor is also important for evaluating its sensing performance. Thus, we periodically measured the CV curves of Cu_2O NCs/NF_{EO} electrodes stored for 1–27 days and obtained the change of response current with the prolongation of storage time (Fig. 5h, Fig. S12). As shown in Fig. 5h, the response signal of Cu_2O NCs/NF_{EO} electrode can retain more than 98.6 % of the initial value even after storing for 27 days, demonstrating its favorable stability. In addition, we also collected the SEM image of Cu_2O NCs/NF_{EO} electrode after detection (Fig. S13), and the well-preserved morphology further indicated its good stability in electrochemical sensing. The desirable reproducibility and stability ensure the reliability of the electrochemical DAH sensor based on Cu_2O NCs/NF_{EO} to be utilized in the analysis of practical samples.

Considering that there are many interfering substances existing in the practical samples, it's essential to ascertain the specificity of Cu_2O NCs/NF_{EO} electrode to exclude the potential signal interference of irrelevant substances. We recorded the I-T curves of Cu_2O NCs/NF_{EO} under the continuous addition of DAH and other interfering substances such as NaCl, KCl, $NaSO_4$, $Zn(NO_3)_2$, $CaCl_2$, Glu, Fru, Suc, Lac etc. in the same concentration (Fig. S14). And according to the corresponding column chart in Fig. 5i, it can be clearly seen that the response current generated by the addition of different interfering substances can almost be ignored, confirming the good selectivity of Cu_2O NCs/NF_{EO} in electrochemical DAH sensing.

The ideal reproducibility, selectivity and stability of proposed sensor based on Cu_2O NCs/NF_{EO} electrode render it enormous potential to be applied for DAH sensing in complex practical environments. DAH added in animal feed or water can react as growth promoting agent, which presents potential health risk to customers [25]. Therefore, the fabricated electrochemical sensor based on Cu_2O NCs/NF_{EO} was applied for the accurate detection of DAH in animal feed. The feasibility of Cu_2O NCs/NF_{EO} for the determination of DAH in actual sample was investigated by the spiked recovery method (Fig. S15). And Table 1 exhibited the satisfying recoveries of Cu_2O NCs/NF_{EO} (91.05–107.78 %) in detecting the DAH concentration in animal feed, which illustrated the excellent reliability of the fabricated sensor based on Cu_2O NCs/NF_{EO} for accurate quantification of DAH in real samples.

Table 1
The electrochemical quantification of DAH in animal feed.

Sample	Added (μM)	Found (μM)	Recovery (%)
1	125	134.72	107.78 ± 2.75
2	250	259.70	103.88 ± 1.23
3	375	364.65	97.24 ± 0.89
4	500	455.27	91.05 ± 2.04

3. Conclusion

In conclusion, a well-defined Cu_2O nanocubes-based electrode with low-index lattice planes was successfully prepared through a green and facile micro-electrolysis strategy. In the pre-processing process of NF, Ni$(OH)_2$ sites were introduced to the surface of substrate and combined with NF to form plenty of micro primary cells, which can tune the nucleation and growth behaviors of Cu_2O nanocrystals and facilitate the formation of Cu_2O nanocubes enclosed with low-index (100) planes. The DFT calculation presented the lowest absorption energy of (100) planes among the low-index facets, which can be ascribed to the electron distribution and charged property. Due to the superior affinity between DAH molecules and the (100) planes of Cu_2O nanocrystals, the Cu_2O NCs/NF_{EO} exhibited favorable electrochemical sensing performance towards DAH, which closely matched the results of DFT calculation. In addition, the reproducibility, stability, selectivity and recovery experiments were also investigated to evaluate the potential of Cu_2O NCs/NF_{EO}-based electrochemical sensor for the detection of DAH, suggesting that the designed electrochemical sensing platform is promising for DAH monitoring in practical samples. This work not only proposes a simple, low-cost and low energy-consumption strategy for the preparation of Cu_2O nanocubes-based sensitive electrochemical sensor, but also reveals the superior planes in DAH sensing among all the low-index planes of Cu_2O nanocubes through DFT calculation, providing new horizon for the design of Cu_2O nanocrystals materials enclosed with low-index facets for electrochemical sensing.

CRediT authorship contribution statement

Yiyue Ma: Writing – original draft, Investigation, Formal analysis, Conceptualization. **Xintong Wu:** Validation, Investigation. **Haoyu Pan:** Validation, Investigation. **Wenxin Zhu:** Supervision. **Chengyi Lu:** Supervision. **Jianlong Wang:** Writing – review & editing, Supervision.

Declaration of competing interest

The authors declare that they have no known competing financial interests or personal relationships that could have appeared to influence the work reported in this paper.

Acknowledgments

We appreciate the kind support from the National Key Research and Development Program of China (No. 2023YFE0103300), the Innovative Talent Promotion Program-Science & Technology Innovation Team of Shaanxi (No. 2023-CX-TD-55), Qinchuangyuan "Scientist + Engineer" team of Shaanxi (2022KXJ-070), Qinghai Special Project of Innovation Platform for Basic Conditions of Scientific Research of China (2022-ZJ-Y18) and the Key Research and Development Program of Shaanxi Province (No. 2022NY-13). We thank the State Key Laboratory of Crop Stress Biology for Arid Areas, Northwest A&F Universiy (Guoyun Zhang) for technical support in SEM analysis.

Appendix A. Supplementary data

Supplementary data to this article can be found online at https://doi.org/10.1016/j.talanta.2024.126995.

Data availability

Data will be made available on request.

References

[1] R.M. Arán-Ais, R. Rizo, P. Grosse, G. Algara-Siller, K. Dembélé, M. Plodinec, T. Lunkenbein, S.W. Chee, B.R. Cuenya, Imaging electrochemically synthesized Cu2O cubes and their morphological evolution under conditions relevant to CO2 electroreduction, Nat. Commun. 11 (1) (2020) 3489.
[2] L. Pan, J.H. Kim, M.T. Mayer, M.-K. Son, A. Ummadisingu, J.S. Lee, A. Hagfeldt, J. Luo, M. Grätzel, Boosting the performance of Cu2O photocathodes for unassisted solar water splitting devices, Nat. Catal. 1 (6) (2018) 412–420.
[3] W. Niu, T. Moehl, W. Cui, R. Wick-Joliat, L. Zhu, S.D. Tilley, Extended light harvesting with dual Cu2O-based photocathodes for high efficiency water splitting, Adv. Energy Mater. 8 (10) (2017) 1702323.
[4] S. Deng, V. Tjoa, H.M. Fan, H.R. Tan, D.C. Sayle, M. Olivo, S. Mhaisalkar, J. Wei, C. H. Sow, Reduced graphene oxide conjugated Cu2O nanowire mesocrystals for high-performance NO2 gas sensor, J. Am. Chem. Soc. 134 (10) (2012) 4905–4917.

[5] T. Gan, Z. Wang, J. Gao, J. Sun, K. Wu, H. Wang, Y. Liu, Morphology–dependent electrochemical activity of Cu2O polyhedrons and construction of sensor for simultaneous determination of phenolic compounds with graphene oxide as reinforcement, Sensor. Actuator. B Chem. 282 (2019) 549–558.
[6] Y. Shang, L. Guo, Facet-controlled synthetic strategy of Cu2O-based crystals for catalysis and sensing, Adv. Sci. 2 (10) (2015) 1500140.
[7] C.-H. Kuo, M.H. Huang, Morphologically controlled synthesis of Cu2O nanocrystals and their properties, Nano Today 5 (2) (2010) 106–116.
[8] M.B. Gawande, A. Goswami, F.-X. Felpin, T. Asefa, X. Huang, R. Silva, X. Zou, R. Zboril, R.S. Varma, Cu and Cu-based nanoparticles: synthesis and applications in catalysis, Chem. Rev. 116 (6) (2016) 3722–3811.
[9] C.H. Kuo, C.H. Chen, M.H. Huang, Seed-mediated synthesis of monodispersed Cu2O nanocubes with five different size ranges from 40 to 420 nm, Adv. Funct. Mater. 17 (18) (2007) 3773–3780.
[10] S. Sun, Z. Yang, Recent advances in tuning crystal facets of polyhedral cuprous oxide architectures, RSC Adv. 4 (8) (2014) 3804–3822.
[11] S. Sun, X. Zhang, Q. Yang, S. Liang, X. Zhang, Z. Yang, Cuprous oxide (Cu2O) crystals with tailored architectures: a comprehensive review on synthesis, fundamental properties, functional modifications and applications, Prog. Mater. Sci. 96 (2018) 111–173.
[12] F.O. Run Liu, Eric W. Bohannan, Frank Ernst, Jay A. Switzer, Shape control in epitaxial electrodeposition: Cu2O nanocubes on InP(001), Chem. Mater. 15 (2003) 4882–4885.
[13] L. Liu, W. Yang, W. Sun, Q. Li, J.K. Shang, Creation of Cu2O@TiO2 composite photocatalysts with p–n heterojunctions formed on exposed Cu2O facets, their energy band alignment study, and their enhanced photocatalytic activity under illumination with visible light, ACS Appl. Mater. Interfaces 7 (3) (2015) 1465–1476.
[14] S. Zhang, X. Mou, Z. Cui, C. Hou, W. Yang, H. Gao, X. Luo, Partial sulfidation for constructing Cu2O–CuS heterostructures realizing enhanced electrochemical glucose sensing, New J. Chem. 45 (16) (2021) 7204–7209.
[15] W.-C. Huang, L.-M. Lyu, Y.-C. Yang, M.H. Huang, Synthesis of Cu2O nanocrystals from cubic to rhombic dodecahedral structures and their comparative photocatalytic activity, J. Am. Chem. Soc. 134 (2) (2011) 1261–1267.
[16] Y. Sui, W. Fu, H. Yang, Y. Zeng, Y. Zhang, Q. Zhao, Y. Li, X. Zhou, Y. Leng, M. Li, G. Zou, Low temperature synthesis of Cu2O crystals: shape evolution and growth mechanism, Cryst. Growth Des. 10 (1) (2009) 99–108.
[17] Y. Deng, A.D. Handoko, Y. Du, S. Xi, B.S. Yeo, In situ Raman spectroscopy of copper and copper oxide surfaces during electrochemical oxygen evolution reaction: identification of CuIII oxides as catalytically active species, ACS Catal. 6 (4) (2016) 2473–2481.
[18] N. Bodappa, M. Su, Y. Zhao, J.-B. Le, W.-M. Yang, P. Radjenovic, J.-C. Dong, J. Cheng, Z.-Q. Tian, J.-F. Li, Early stages of electrochemical oxidation of Cu(111) and polycrystalline Cu surfaces revealed by in situ Raman spectroscopy, J. Am. Chem. Soc. 141 (31) (2019) 12192–12196.
[19] Y. Yang, L. Li, G. Ruan, H. Fei, C. Xiang, X. Fan, J.M. Tour, Hydrothermally formed three-dimensional nanoporous Ni(OH)2 thin-film supercapacitors, ACS Nano 8 (9) (2014) 9622–9628.
[20] K.-D. Kim, J.W. Nam, H.O. Seo, Y.D. Kim, D.C. Lim, Oxidation of toluene on bare and TiO2-covered NiO-Ni(OH)2 nanoparticles, J. Phys. Chem. C 115 (46) (2011) 22954–22959.
[21] H. Cui, X. Yan, B. Liu, X. Zhao, X. Zhang, X. Zhao, X. Tong, Y. Wang, Y. Xing, Flower-like spherical Ni-benzimidazole derived Ni-NiO-C complexed with carbon nanotubes as electrocatalysts for lithium-sulfur battery, J. Alloys Compd. 931 (2023) 167402.
[22] X. Wang, X. Liu, J. Fang, H. Wang, X. Liu, H. Wang, C. Chen, Y. Wang, X. Zhang, W. Zhu, Z. Zhuang, Tuning the apparent hydrogen binding energy to achieve high-performance Ni-based hydrogen oxidation reaction catalyst, Nat. Commun. 15 (1) (2024) 1137.
[23] S. Singha Roy, R. Madhu, K. Bera, S. Nagappan, H.N. Dhandapani, A. De, S. Kundu, Tuning the activity and stability of CoCr-ldh by forming a heterostructure on surface-oxidized nickel foam for enhanced water-splitting performance, ACS Appl. Mater. Interfaces 16 (5) (2024) 5965–5976.
[24] H. Guo, Y. Chen, H. Ping, J. Jin, D.-L. Peng, Facile synthesis of Cu and Cu@Cu–Ni nanocubes and nanowires in hydrophobic solution in the presence of nickel and chloride ions, Nanoscale 5 (6) (2013) 2394–2402.
[25] M. Chen, W. Li, H. Xiong, W. Wen, X. Zhang, S. Wang, Discrimination and ultrasensitive detection of β2-agonists using copper nanoclusters as a fluorescent probe, Microchim. Acta 184 (2017) 3317–3324.

Advanced Composites and Hybrid Materials (2025) 8:342
https://doi.org/10.1007/s42114-025-01422-x

RESEARCH

Multipurpose biosensing electronics enabled by ultrasoft and durable hydrogel via ions pre-incorporation

Yiyue Ma[1] · Congdi Shang[1] · Yiting Xu[1] · Xintong Wu[1] · Wenxin Zhu[3] · Wenzhi Tang[1] · Hai Tan[2] · Jianlong Wang[1]

Received: 4 April 2025 / Revised: 15 July 2025 / Accepted: 11 August 2025

Abstract
Fast-growing flexible electronics bring technological innovation to all industries, including personal health management, clinical diagnosis, and smart agriculture. However, conventional synthesis strategy fails to reconcile the divergent mechanical property demands for monitoring disparate targets (such as humans and plants), impeding the development of a universal strain sensor. In this work, a universal ions pre-incorporation strategy is first proposed to develop ultrasoft and durable ionic hydrogels for multipurpose biosensing. Through iron-mediated Fenton-like reactions and Cl^--dominated radical scavenging effects, the glycerin-doped PAAM/PVA hydrogel pre-incorporated with Fe ions (GPPFe) exhibits ultrasoft mechanical properties (Young's modulus = 41.7 kPa, 84.8% softer than post-incorporated samples), effectively avoiding the excessive stiffness of ionic hydrogels prepared by the conventional ions post-incorporation strategy, which can be well applied for the monitoring of plant growth considering its good conformal contact with the plant surface and less pressure on the plant tissues. The reversible and sacrificial bonds formed between Fe^{3+} and polymers ensure excellent mechanical stability of the GPPFe hydrogel (1.12% permanent deformation after successive loading–unloading 50 cycles test at a tensile strain of 150%, 94.7% lower than post-incorporation strategy), thus ensuring its utilization as a comfortable and durable human wearable strain sensor. Additionally, this strategy can be extended to design various types of synthetic hydrogels, providing an innovative approach for designing the multipurpose wearable electronic devices oriented to various target objects.

Keywords Ultrasoft hydrogel · Wearable sensor · Ions pre-incorporation · Multipurpose biosensing

1 Introduction

The in-time and accurate monitoring of biological activities can efficiently transfer the information associated with body conditions of individual organisms and contribute to biological health assessments. [1–3] For example, real-time monitoring of diverse human motions can be employed for the record of the frequency of human movement as well as the prevention and diagnosis of some neurodegenerative disorders-related diseases, which is of great significance for further evaluation about human health status. In addition, real-time monitoring of plant growth, including growth rate and abnormal growth, as an important part of precision agriculture, provides an effective way for increasing crop yields and improving agricultural production. However, the current state-of-the-art of strain sensors demonstrates poor universality and are generally applied to a single target object only (human or plant). The reason lies in the significant differences in the requirements of sensing materials in different biological activities monitoring. In practice, the demand for comfort level and durability in human wearable strain sensors requires soft materials with good deformability and excellent antifatigue property, while the requirement for low Young's modulus is higher in plant monitoring since we desire to accomplish the monitoring of plant growth under

✉ Wenzhi Tang
tangwenzhi@nwsuaf.edu.cn

✉ Hai Tan
Doc.tan@outlook.com

✉ Jianlong Wang
wanglong79@nwsuaf.edu.cn

[1] College of Food Science and Engineering, Northwest A&F University, 22 Xinong Road, Yangling, Shaanxi 712100, China

[2] College of Mechanical and Electronic Engineering, Northwest A&F University, 22 Xinong Road, Yangling, Shaanxi 712100, China

[3] School of Materials Science and Engineering, Peking University, Beijing 100871, China

Published online: 28 August 2025

the fewest possible compression. The pronounced discrepancy between the required properties in human body monitoring and plant monitoring poses a serious challenge to the design of versatile multipurpose biosensors.

Currently, most research on strain sensors is focused on the exploitation of sensing systems for human activity monitoring. There are some common strategies such as (1) rigid conductive material with designed geometric structure, (2) material with intrinsic high elongation and conduction, and (3) stretchable/flexible elastomer substrates incorporated with conductive material or electronic components. [4–6] Compared with rigid materials, hydrogel, as a kind of soft material consisting of a 3D elastic polymer network, can efficiently avoid fundamental mismatch between rigid sensors and soft biological tissues. [7–11] Among them, ionic conductive hydrogels utilize electrically conductive and water-soluble ionic electrolytes that offer natural compatibility advantages with hydrophilic polymer networks, exhibiting promising potential to be utilized for flexible electronics owing to their high stretchability, biocompatibility, and wearing comfort. However, at present, ionic hydrogels are generally obtained through a post-incorporation strategy, which introduces metal ions by immersing the hydrogel substrate into a salt-containing solution. Due to the salting-out effect induced by salt solutions, hydrogels obtained by the ion post-incorporation strategy usually possess excessive tensile strength, Young's modulus (generally to hundreds of kilopascals), and toughness as well as reduced resilience, which is unable to satisfy the requirements for durability in human motion monitoring and for non-compression in plant growth monitoring. Therefore, the design of versatile multipurpose biosensors remains a serious challenge.

In this work, we proposed a simple ions pre-incorporation strategy to prepare ultrasoft glycerin-doped hydrogel of PAAM/PVA pre-incorporated with Fe ions (GPPFe) with low Young's modulus (41.7 kPa) and good mechanical stability (1.12% permanent deformation after successive loading–unloading 50 cycles test at a tensile strain of 150%), which can simultaneously satisfy the sensing demand in various application scenes. Specifically, we constructed an interpenetrating polymer networks (IPNs) hydrogel consisting of PVA and PAAM, and the PAAM network formed through free radical polymerization induced by APS while the PVA network was synthesized after freezing–thawing cycles. During the synthesis process, Fe ions are incorporated into the precursor matrix in advance, which can not only act as ion conductors but also play an important role in adjusting the physicochemical property of the G-PAAM/PVA IPNs hydrogel. [12, 13] The pre-incorporated Fe ions can be well integrated into the matrix and entangle between the polymer chains through coordination interactions, and thus provide an effective mechanism for dissipating energy and ensure the favorable mechanical stability in a large range of movement and frequent usage in human activity monitoring. Meanwhile, the degree of polymerization is modulated through the equilibrium between iron-mediated Fenton-like reactions and Cl^--dominated radical scavenging effect. Under the optimum concentration of pre-incorporated ions, we can efficiently avoid the undesired high stiffness existing in ions post-incorporated hydrogels, contributing to an ultrasoft mechanical property appropriate for plant growth monitoring. The strategy proposed in this work offers a new versatile way on the development of ionic conductive hydrogels, providing promising insights for the fabrication of universal flexible wearable sensors oriented to multiple objects.

2 Results and discussions

As exhibited in Fig. 1a, in this work, we aim to address this need by resolving the mechanical incompatibility between human- and plant-targeted sensors through a pre-incorporation methodology for embedding Fe^{3+} ions into glycerin-doped PAAM/PVA hydrogels (GPPFe). To this end, the prepared hydrogels should bypass the rigidity induced by salt-out effects in traditional post-incorporation methods, achieving an ultrasoft mechanical property while ensuring conformal contact with delicate plant surfaces and minimizing tissue compression (Fig. 1b). Simultaneously, the hydrogel should be engineered with excellent mechanical stability to ensure ideal performance in long-term monitoring of human motion. For all IPN hydrogels, the PAAM covalent crosslinked network was formed in situ before the PVA crystalline domain network was constructed, regardless of the presence or absence of Fe(III) ions. For the Fe^{3+}-absent IPN hydrogel of G-PAAM/PVA, it was first formed by free radical polymerization of AAM monomer and MBAA crosslinker under APS thermal initiation to form a single-network (SN) hydrogel of PAAM (PAAM SN), where the free PVA chains formed a PVA single network (PVA SN) after three freeze–thaw cycles, as shown in Fig. 1b. The freezing step leads to the separation of the water-polymer phase and the aggregation in the polymer-rich phase and the formation of polymer crystals of PVA chains, which can act as crosslinks between the chains and promote the formation of PVA networks ultimately leading to IPN hydrogels. [14] For the IPN hydrogels pre-incorporated with Fe^{3+} (GPPFe), they were named $GPPFe_{0.07\ M}$, $GPPFe_{0.2\ M}$, and $GPPFe_{0.33\ M}$, respectively, according to the concentration of Fe^{3+}, e.g., the sample $GPPFe_{0.2\ M}$ implies that the concentration of Fe^{3+} is 0.2 M. In addition, $GPPFe_{0.2\ M\ post}$ was prepared from IPN hydrogel of G-PAAM/PVA immersed in 0.2 M Fe^{3+} solution. For comparison, the PVA SN hydrogel was also prepared by freeze–thaw cycles using a PVA solution without PAAM network constituents and Fe^{3+}.

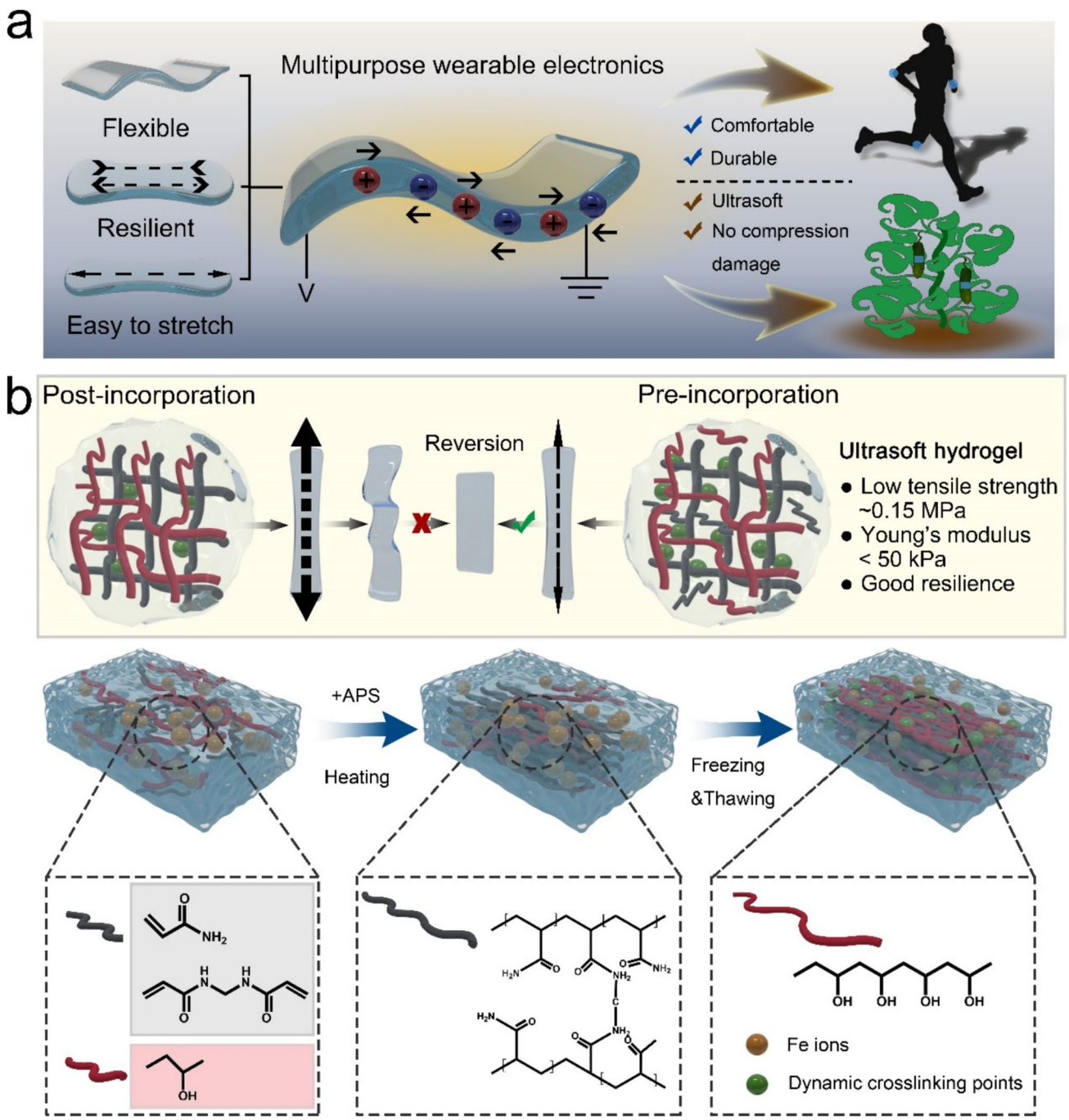

Fig. 1 **a** GPPFe-based multipurpose wearable sensors for human motion and plant growth monitoring. **b** Schematic illustration of the preparation of the GPPFe hydrogel and its advantages compared with ion post-incorporation strategy

The gelation processes of different hydrogels can be observed from optical pictures, as displayed in Figure S1. The pure PVA solution was gelled after undergoing one freeze–thaw cycle and formed a stable hydrogel after performing three freeze–thaw cycles, suggesting that our preparation method does favor the construction of the PVA SN. For the IPN hydrogels of G-PAAM/PVA, a SN hydrogel of PAAM was formed after only heating, and further freeze–thaw cycles reduced the transparency of the gel, proposing the successful construction of these two interpenetrating networks. However, after pre-addition of $FeCl_3$ to the G-PAAM/PVA system, the hydrogels could not be formed by merely heating, which could be attributed to the $FeCl_3$ acting as a depolymerizing agent that quenches the free radicals, [11] resulting in the prevention of PAAM from forming a complete network to gel the aqueous solution.

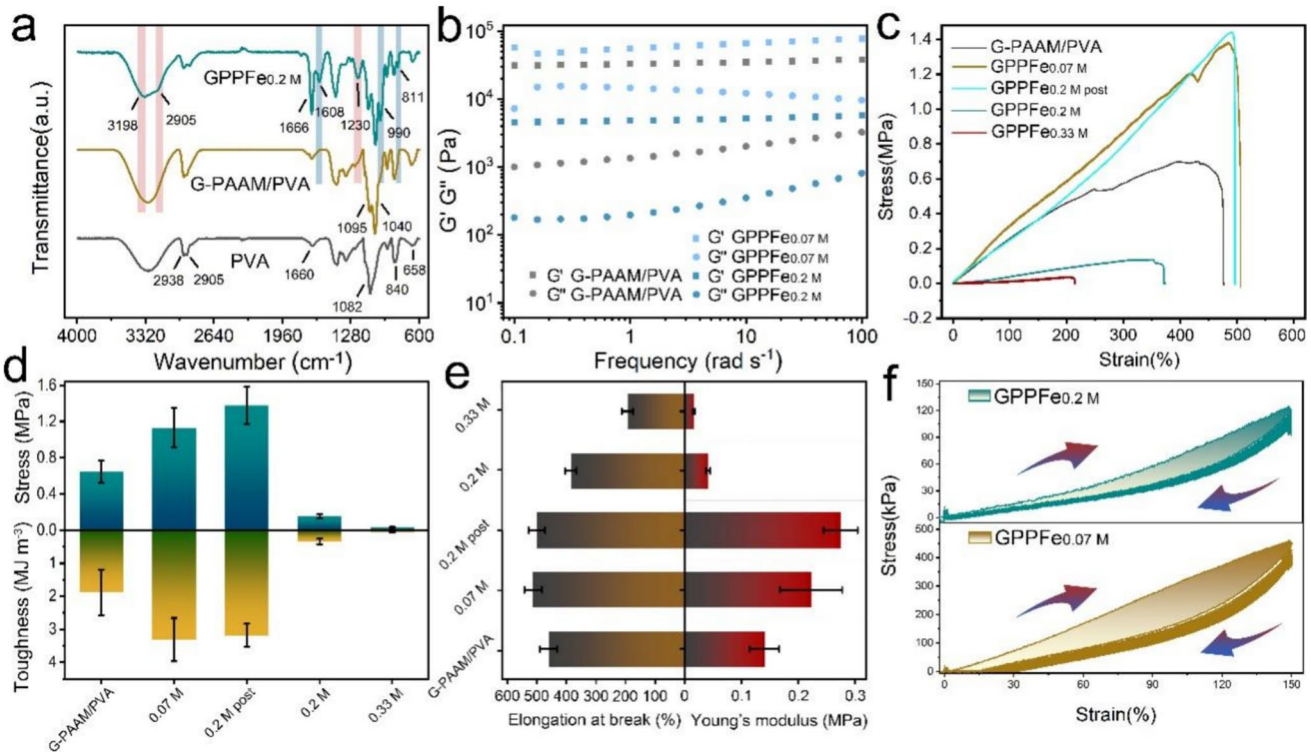

Fig. 2 **a** FTIR spectra of PVA SN, G-PAAM/PVA IPN, and $GPPFe_{0.2\ M}$ hydrogels. **b** G′ and G″ as a function of frequency for G-PAAM/PVA IPN, $GPPFe_{0.07\ M}$ and $GPPFe_{0.2\ M}$ hydrogels. **c** Tensile stress–strain curves of IPN hydrogels of G-PAAM/PVA and incorporated with various content of Fe^{3+} (GPPFe). **d** Corresponding breaking stress and fracture energy of different hydrogels. **e** Corresponding elongation at break and Young's modulus of different hydrogels. **f** Successive loading–unloading curves of the $GPPFe_{0.07\ M}$ and $GPPFe_{0.2\ M}$ hydrogels under 150% tensile strain for 50 cycles

This suggests that the pre-incorporation of $FeCl_3$ is detrimental to the formation of both PAAM and PVA networks. In other words, the degree of cross-linking of the IPN hydrogel network can be controlled by modulating the amount of pre-integrated $FeCl_3$, thereby modulating the mechanical properties of the conductive hydrogels.

To characterize the successful synthesis of GPPFe hydrogel, the FT-IR spectra of PVA SN, G-PAAM/PVA IPN, and GPPFe hydrogels were collected in the range of 4000 ~ 600 cm^{-1} to explore the chemical bonding configurations of prepared samples (Fig. 2a). The broad band (3180 ~ 3400 cm^{-1}) that appears in all samples is related to the overlap of the O–H stretching and N – H characteristic peaks. [15–17] In the FT-IR spectrum of PVA SN hydrogel, the peaks located at 1082 and 658 cm^{-1} can be assigned to C-O and O–H twist, respectively. [18–20] And after the introduction of PAAM, there are two peaks observed at 1040 and 1095 cm^{-1}. Thereinto, the peak at 1040 cm^{-1} corresponds to -NH_2 in-plane rocking vibrations, while the peak at 1095 cm^{-1} can be ascribed to the overlap of C – N and C – O stretching vibration. [21–23] Besides, the intensity of peaks at 2938, 2905, and 840 cm^{-1} in the FT-IR spectrum of PVA SN hydrogel significantly increases accompanied by the addition of PAAM, which corresponds to the CH_2 asymmetric stretching, C–H stretching, and CH_2 asymmetric rocking motion with some contribution of C-O stretching. [24] The above results indicated the successful introduction of PAAM chains and their effective combination with PVA chains through interactions between chain segments. In the FT-IR spectrum of $GPPFe_{0.2\ M}$, a new peak located at 811 cm^{-1} can be observed, which refers to the formation of Fe–O bond. [25] Another newly emerging peak at 990 cm^{-1} is related to C-O stretching vibration. [26] The peak located at 1608 cm^{-1} also emerges after the insertion of Fe^{3+}, which can be ascribed to the bending vibrations of N–H from amide II from the α – helix secondary structure. [27] Therefore, we can find that the Fe^{3+} binds to G-PAAM/PVA polymer chains through Fe – O bonds and affects the interaction of the polymers. In addition, the intensity of the peak at 1666 cm^{-1} significantly increases, which is related to the C = O bond stretching vibration of amide I and C = C stretching, suggesting the decrease of the degree of polymerization after the introduction of $FeCl_3$. [28] The peaks located at 3198 (O–H stretching), 2905 cm^{-1} (C–H stretching), and 1230 cm^{-1} (C – N stretching vibrations) exhibited significant red shift, indicating the addition of hydrogen

bond interactions between chains induced by added Fe^{3+}. [29]

To demonstrate the regulating role of introduced Fe^{3+} on the mechanical properties of IPN hydrogel of G-PAAM/PVA, rheological tests were first performed to learn about their oscillatory mechanical behaviors. As illustrated in Fig. 2b, the storage modulus (G′) is consistently higher than the loss modulus (G″) over all tested frequency (ω) ranges, which indicates that the IPN hydrogels of G-PAAM/PVA and all GPPFe are solid-like stable hydrogels. With a small amount of Fe^{3+} (0.07 M), the plateau elastic modulus (66,442 Pa) of the $GPPFe_{0.07\ M}$ hydrogel increased slightly compared to G-PAAM/PVA IPN hydrogel (34,770 Pa), suggesting that the weak interaction of Fe(III) with the two networks indeed increases the cross-linking density of the IPN system and thus the mechanical strength of the hydrogel. However, as we observed earlier (Figure S1), pre-added Fe^{3+} reduces the number of cross-links in the two networks of the IPN, which is the main contributor to the elastic moduli of the gels. Thus, even with the pre-incorporation of only 0.2 M of Fe^{3+} into our G-PAAM/PVA IPN hydrogel, the plateau modulus of $GPPFe_{0.2\ M}$ (5129 Pa) still showed a more significant decrease. The difference in oscillatory mechanical properties between $GPPFe_{0.07\ M}$ and $GPPFe_{0.2\ M}$ further suggests that although $FeCl_3$ can increase the cross-linking density of the IPN system, the higher the concentration of pre-added $FeCl_3$ the more it harms the integrity of the two sub-networks of the IPN. Overall, the elastic moduli of these GPPFe IPN hydrogels are relatively close to those of many soft parts of the human body and plants, [30–32] and can be developed into soft sensing devices for them.

Except for the elastic modulus, conductive hydrogels as wearable sensors should also have suitable deformation ability. As shown in Figure S2, the proposed ionic conductive hydrogel can withstand various deformations including stretching and knotting. For this purpose, we carried out mechanical tests on the prepared IPN hydrogels, and the tensile stress – strain behaviors of IPN hydrogels of G-PAAM/PVA and GPPFe were investigated. Similar to the rheological results, the introduction of Fe^{3+} into the IPN without (or less) affecting the formation of the two sub-networks of the IPN as much as possible would improve the mechanical properties of the hydrogels. As shown in Fig. 2c, the tensile strength and strain at break of $GPPFe_{0.07\ M}$ with a small amount of pre-incorporated Fe^{3+} and $GPPFe_{0.2\ M\ post}$ introducing Fe^{3+} after gel formation were significantly higher than those of G-PAAM/PVA IPN hydrogel. Moreover, the fracture energy (Fig. 2d) and Young's modulus (Fig. 2e) of $GPPFe_{0.07\ M}$ and $GPPFe_{0.2\ M\ post}$ were also significantly higher than those of G-PAAM/PVA IPN hydrogel, which further demonstrated that the formation of reversible cross-links by Fe^{3+} in IPN is favorable for energy dissipation and thus enhances the mechanical performances of the hydrogels. However, the hydrogels with high toughness are not applicable for non-destructive monitoring of plant growth. [33] To obtain IPN hydrogels with suitable flexibility and better ionic conductivity, we also tested the mechanical properties of $GPPFe_{0.2\ M}$ and $GPPFe_{0.33\ M}$ hydrogels that were pre-integrated with more Fe^{3+} (Figs. 2c–e). The maximum tensile stress of $GPPFe_{0.2\ M}$ hydrogel was 0.15 MPa with a fracture strain of 385% and fracture energy of 0.34 MJ m^{-3}. Furthermore, its elastic modulus value is approximate to some native soft tissues from humans and plants, which is significantly lower than common commercial soft materials, ensuring its suitability for further flexible sensing applications (Tables S1–S2). However, with the content of $FeCl_3$ increased to 0.33 M, the disruption of the hydrogel network causes decreased mechanical property (tensile stress < 0.031 MPa and elongation at break < 193.3%), which is unsuitable for practical applications. The modulation of polymerization is primarily achieved through the equilibrium between iron-mediated Fenton-like reactions and Cl^--dominated radical scavenging effect. By analogy to the Fenton system, there is a Fenton-like system existing between iron ions and persulfate. In our synthesis system, it is suggested that a comparable Fenton-like reaction occurs in the following way. In the initial phase when persulfate is added to the system, Fe(III) can be reduced to Fe(II) under the presence of co-existing substances (acrylamide monomer, SO_2 et al.) within the system. [34] Then Fe (II) can react with $S_2O_8^{2-}$ to generate Fe (III), SO_4^{2-}, and thus introduce iron-mediated Fenton-like reaction. [35] During this process, a transformation of Fe(III) to Fe(IV) simultaneously occurs in the system. [36] The above process is conducive to the generation of radicals with high reactivity and accelerates the polymerization of PAAM networks, resulting in enhanced mechanical property. However, as $FeCl_3$ concentration increases, insufficient Fe(II) is available for Fenton-like reaction due to limited reducing substances in the system. At the same time, Cl^- in the system has a negative effect on the above process through the quenching effect on SO_4^- radicals, disrupting the integrity of the hydrogel network. [37] The Fenton-like reaction dominated by iron ions and the reaction dominated by chloride ions for radical scavenging together affect the formation of PAAM networks based on free radical polymerization and thus adjusting the mechanical properties of GPPFe hydrogels. The critical concentration for hydrogel network disruption was also investigated by tube inversion test (Figure S3). Glycerin in GPPFe hydrogels can enhance the toughness and increase the elongation at break of hydrogels (Figure S4), and thus avoid too low mechanical properties and the resulting poor practicality.

To show the fatigue resistance of $GPPFe_{0.2\ M}$ hydrogel for flexible sensing applications, we tested its successive loading–unloading stretching at a strain of 150% (less than the corresponding tensile rupture strain) for 50 cycles and compared it with other hydrogels (Fig. 2f and Figure S5). Compared to $GPPFe_{0.07\ M}$ and $GPPFe_{0.2\ M\ post}$ hydrogels, the hysteresis loop of the $GPPFe_{0.2\ M}$ hydrogel is much smaller, suggesting that the $GPPFe_{0.2\ M}$ system allows for efficient energy dissipation and thus less energy loss during successive loading–unloading tensile processes. Moreover, $GPPFe_{0.2\ M}$ exhibited a permanent deformation as low as 1.12% after 50 stretching cycles, significantly lower than other IPN hydrogels with better tensile mechanical properties ($GPPFe_{0.07\ M}$: 25.9%, $GPPFe_{0.2\ M\ post}$: 21%) (Figure S5). Then, the fatigue tests were further extended to 1000 cycles under conditions of 25 °C and 75% relative humidity (Figure S6). At low strains (30%), the $GPPFe_{0.2\ M}$ hydrogel consistently maintained high structural stability throughout the cycles, demonstrating excellent recoverability and minimal hysteresis loss, which is crucial for applications requiring repeated small deformations. Even with the applied strain increased to 100%, there is almost no permanent deformation at the end of the test. Furthermore, we measured the successive loading–unloading stretching of $GPPFe_{0.2\ M}$ hydrogel for 1000 cycles under controlled varying temperature (20, 25, and 30 ℃) and humidity (50%, 75%, and 90%) conditions to investigate the effects of environmental factors. As shown in Figures S7–S8, across all the temperature and humidity conditions, the permanent deformations at the end of the test were negligible, indicating good fatigue resistance in different environmental conditions. These results further imply that $GPPFe_{0.2\ M}$ hydrogel with suitable mechanical strength and deformation capacity has better self-recovery and fatigue resistance and is particularly suitable for flexible sensing applications.

Considering the significant effect of gel structure on the mechanical properties of the prepared hydrogels, SEM images and X-ray photoelectron spectroscopy (XPS) were collected to obtain the surface texture and additional structural insight. The SEM image of SN hydrogel of PVA in Figure S9 exhibits a relatively compact and smooth surface. After the incorporation of PAAM network, the IPN hydrogel of G-PAAM/PVA displays a gluten network-like structure with an enlarged pore size and its surface getting rougher (Fig. 3a), which can be ascribed to the disruption of the compact structure of PVA chains induced by the interpenetrated PAAM network. A small amount of Fe^{3+} pre-introduced into the system did improve the cross-linking density of the IPN hydrogels; and thus, $GPPFe_{0.07\ M}$ (Fig. 3b) exhibited a denser network morphology compared to G-PAAM/PVA IPN hydrogel. For the IPN hydrogel of $GPPFe_{0.2\ M}$, a large number of particles were uniformly distributed on the porous structure of the hydrogel network, probably originating from the ferric salts, which would undoubtedly greatly increase the ionic conductivity of the hydrogel. Moreover, as discussed earlier in the mechanical part, $GPPFe_{0.2\ M}$ has a lower cross-linking density compared to $GPPFe_{0.07\ M}$ due to the pre-addition of a large amount of $FeCl_3$ partially disrupting the formation of the two sub-networks of the IPN. Accordingly, the gel network of $GPPFe_{0.2\ M}$ is more loose and penetrating, which may be more favorable for ion transport of the conductive electrolyte.

Then the surface chemical compositions of different hydrogels were analyzed by XPS spectra. As shown in Figure S10, in the XPS survey spectra, all samples contain C and O as the main elements, and the diffraction peaks related to N and Fe elements emerged after the incorporation of PAAM and $FeCl_3$, respectively. High-resolution core-level scans were also conducted to obtain detailed information on surface compositions. High-resolution O 1 s spectra in Fig. 3d revealed the appearance of C = O in IPN hydrogel of G-PAAM/PVA and $GPPFe_{0.2\ M}$ apart from the C – O and – OH in SN hydrogel of PVA, which indicated the incorporation of PAAM. In addition, a new peak located at 530.7 eV emerged in the high-resolution O 1 s spectrum of $GPPFe_{0.2\ M}$ hydrogel, which can be ascribed to the formation of M – O bond between Fe^{3+} and the network of G-PAAM/PVA IPN hydrogel. For C 1 s spectra, the peaks observed at 284.5, 286.0, and 287.8 eV can be attributed to the C atoms in C – C/C=C, C – O/C – N, and C=O groups, respectively. [38] The emergence of the peak at 286.0 eV attributed to the C=O demonstrated the successful incorporation of PAAM into the network of PVA SN hydrogel. Compared with IPN hydrogel of G-PAAM/PVA, the peaks related to C–O, C–N, and –OH shifted to lower binding energy in the high-resolution O 1 s spectrum of $GPPFe_{0.2\ M}$ hydrogel, demonstrating the formation of hydrogen bond interactions between Fe^{3+} and the networks of IPN hydrogels. [39] And in the spectrum of N 1 s of $GPPFe_{0.2\ M}$, there are four characteristic peaks appearing at 399.0, 399.7, 400.6, and 401.9 eV, corresponding to the – N=, – NH –, $-NH_2$ and $-NH^+-$ respectively (Fig. 3e). [40, 41] The peak related to the $-NH^+-$ can be ascribed to the peroxidation of AAM under the action of oxidizing agent. [42] It can be observed that the signal intensity of $-NH^+-$ and $-NH_2$ gradually increases when increasing the content of $FeCl_3$, which can be attributed to the addition of excess oxidants and exposure of monomer molecules, indicating the decreased degree of polymerization of PAAM in GPPFe hydrogel (Figure S11).

The PAAM and PVA networks of IPN hydrogels are abundant in hydroxyl and amine groups, which are able to act on other surfaces via hydrogen bonding, coordination bonding, and so on (Fig. 3 g), and thus the hydrogels exhibit a definite adhesion property. As shown in Fig. 3 h, the $GPPFe_{0.2\ M}$ hydrogels can be adhered to the surface of

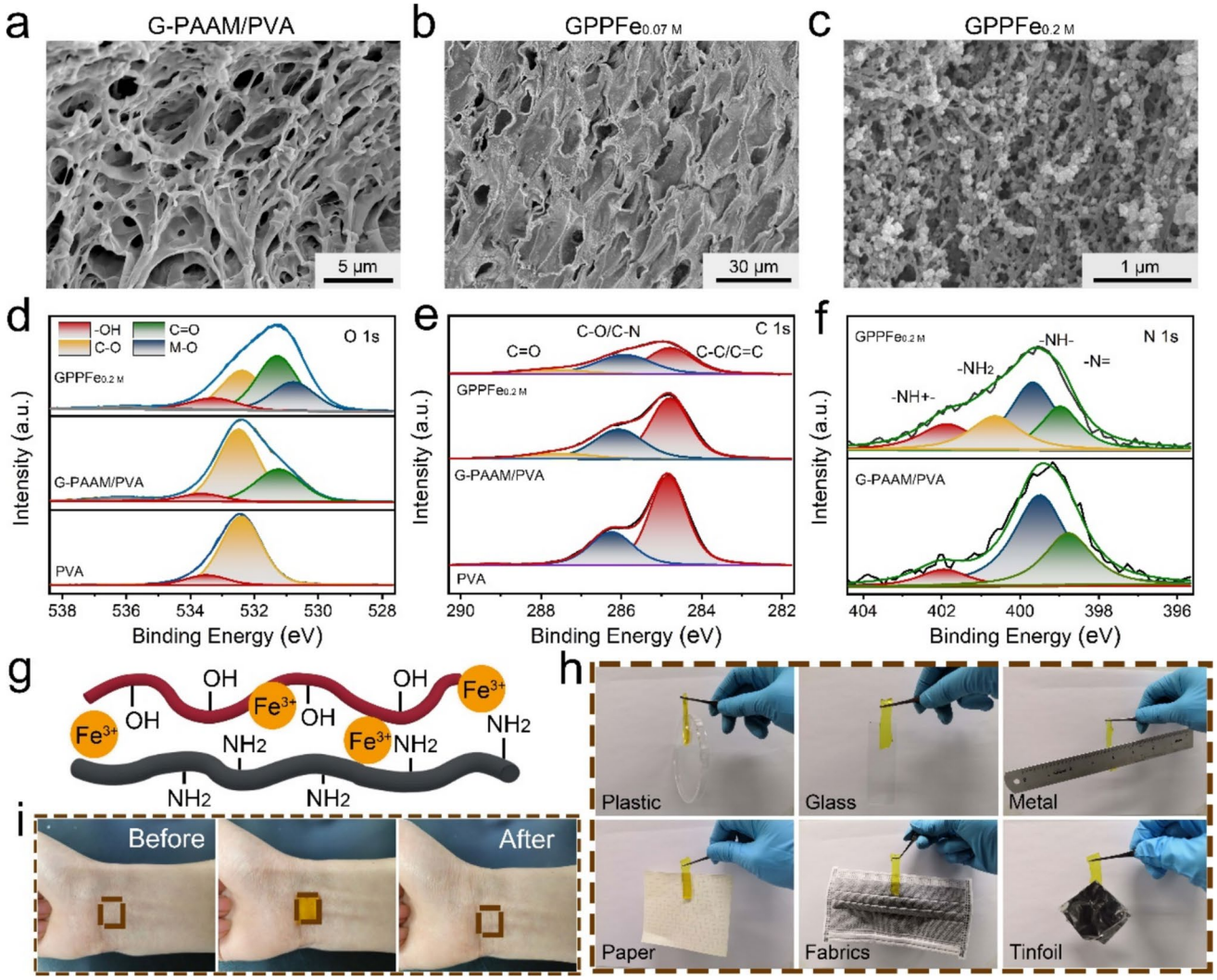

Fig. 3 **a–c** SEM images of IPN hydrogels of G-PAAM/PVA (**a**), $GPPFe_{0.07\ M}$ (**b**), and $GPPFe_{0.2\ M}$ (**c**). d-e XPS O 1 s spectra (**d**) and XPS C 1 s spectra (**e**) of SN hydrogel of PVA, IPN hydrogel of G-PAAM/PVA, and $GPPFe_{0.2\ M}$. **f** XPS N 1 s spectra of IPN hydrogel of G-PAAM/PVA and $GPPFe_{0.2\ M}$. **g** Schematic diagram of the surface functional groups of $GPPFe_{0.2\ M}$ that contribute to adhesion property. **h** Adhesion property of $GPPFe_{0.2\ M}$ to different substrates. **i** Photographs of $GPPFe_{0.2\ M}$ peeled off from skin without residue

different objects such as plastic, glass, fabric, paper, metal, and tinfoil, which fully demonstrates the potential of hydrogels to be applied in a variety of practical fields. In addition, after being adhered to the human skin, the $GPPFe_{0.2\ M}$ hydrogel can be easily peeled off with no residue and no anaphylactic reaction (Fig. 3i), making it promising in biosensing.

The conductivity properties of our IPN hydrogel of GPPFe are mainly dependent on the iron salt electrolyte. The permeable network structures and enhanced water retention properties of IPN hydrogel of GPPFe can provide abundant channels for the migration of electrolyte ions, contributing to the construction of ionic conductive hydrogels. Therein, the concentration of salts added into the hydrogel can efficiently alter its conductivity, which can be verified through the measurement of electrochemical impedance spectroscopy (EIS) in Fig. 4a. Further, the conductivity values of hydrogels prepared with different pre-addition of Fe^{3+} were calculated by Nyquist plot using the same equivalent circuit, and the results are presented in Fig. 4b. We can find that the ionic conductivity is significantly improved with the increase of Fe(III) ion content in the GPPFe hydrogels.

The GPPFe conductive hydrogel was used as a conductor to connect an electric circuit with a light-emitting diode (LED) bulb as an indicator. To investigate the electrical recovery ability of GPPFe hydrogel, we cut off the hydrogel in the series circuit and then recontacted it. It can be observed that the LED bulb was lit up when a complete hydrogel was accessed in the circuit while the glowing bulb went out with separated two segments of hydrogel. But if we made the two parts of hydrogel reconnected again, the

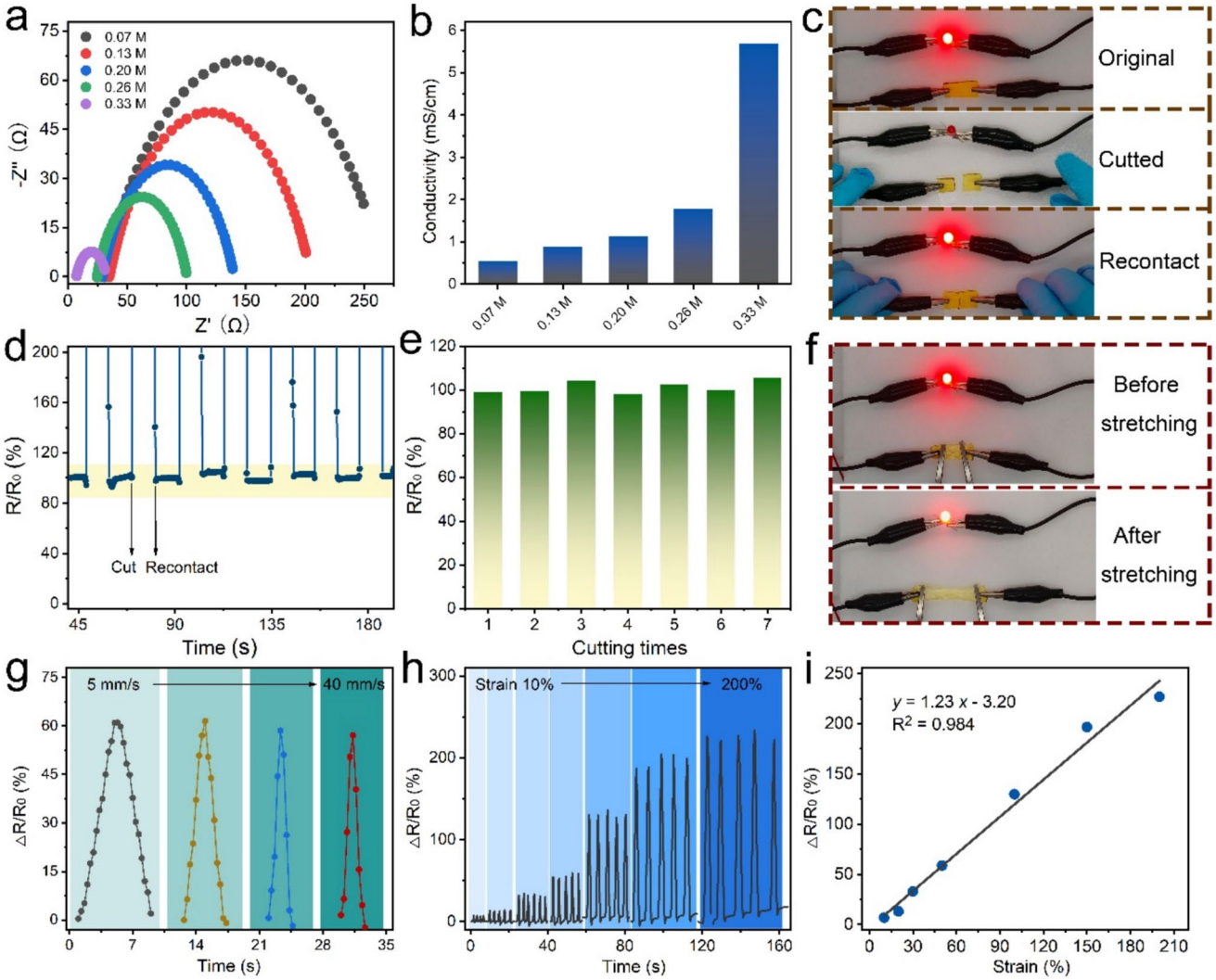

Fig. 4 **a** EIS curves of the GPPFe hydrogels incorporated with different contents of Fe ions. **b** Corresponding conductivity calculated from EIS curves. **c** Photographs of LED luminance change in response to the stretching of $GPPFe_{0.2\ M}$ hydrogel. **d** Real-time resistance changes of $GPPFe_{0.2\ M}$ hydrogel in cutting-recontacting cycles. **e** The recovering efficiency of electrical conductivity during cutting-recontacting cycles. **f** Photographs of LED luminance change in response to the stretching of $GPPFe_{0.2\ M}$ hydrogel. **g** Relative resistance changes of $GPPFe_{0.2\ M}$ hydrogel under different stretching speeds with a strain of 50%. **h** Relative resistance changes of $GPPFe_{0.2\ M}$ hydrogel under cyclic stretching with different strain. **i** Relative resistance changes of $GPPFe_{0.2\ M}$ hydrogel as a function of applied strain

bulb still would be immediately lit up like before (Fig. 4c). This result manifested the good conductive recovery ability of GPPFe conductive hydrogel, which can also be verified through the dynamic resistance curves in Fig. 4d. The results indicated that after the hydrogel was cut off, the measured resistance of conductive hydrogel increased sharply and exceeded the range of the meter due to the infinite resistance of air. And the resistance of the hydrogel returned to the initial value once we recontacted the separated two parts of hydrogel (Fig. 4e).

In addition, the brightness of the LED bulb got dimmed when stretching the GPPFe hydrogel, reflecting the strain-dependent responsiveness of the hydrogel (Fig. 4f). It can be ascribed to the fact that during the stretching process, the resistance of the hydrogel will increase due to the narrower ion channel and elongated migration path, based on which we can realize the sensitive response to stretching and monitoring of the geometric deformation under external forces. The relative resistance changes of $GPPFe_{0.2\ M}$ hydrogel under different stretching speeds were also conducted at a strain of 50%, and the result indicated the favorable stability of the strain sensor based on $GPPFe_{0.2\ M}$ hydrogel under different tension speeds (Fig. 4 g). To evaluate the strain sensing performance of GPPFe conductive hydrogels, we collected the real-time change of the resistance (R) under different-length uniaxial tensile stretching. As shown

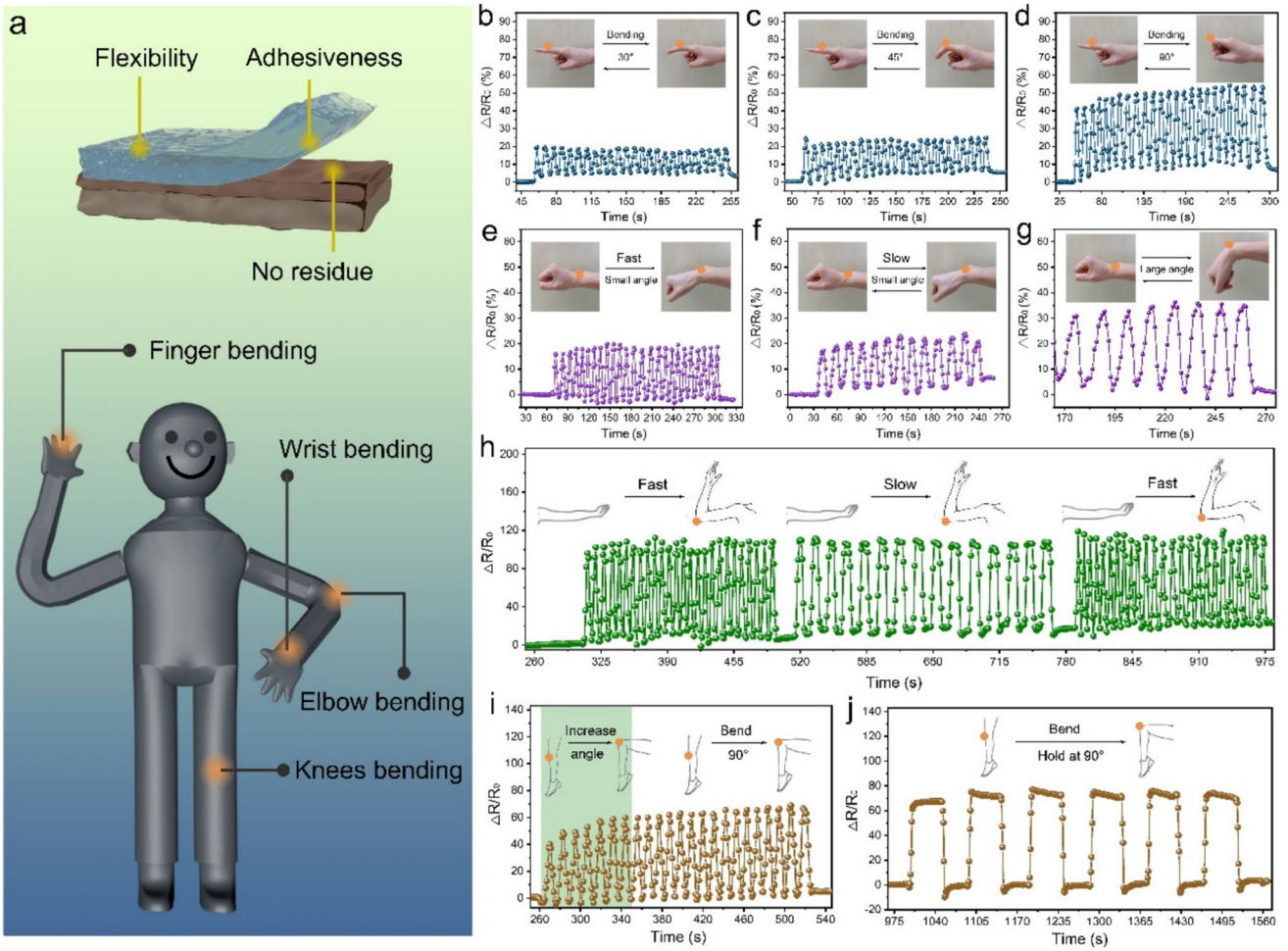

Fig. 5 **a** Application in human activities monitoring of the $GPPFe_{0.2\ M}$ hydrogel. **b–j** Real-time resistance changes collected during different behaviors: **b–d** finger bending, **e–g** wrist bending, **h** elbow bending, **i–j** knee bending

in Fig. 4 h–i, the resistance of $GPPFe_{0.2\ M}$ hydrogel gradually increased with the continuously growing tensile strain. Accordingly, the gauge factor (GF) of $GPPFe_{0.2\ M}$ hydrogel value was calculated as 1.23 in the strain of 10% ~ 200%. Compared with other ionic conductive hydrogels-based strain sensors (Table S3), our GPPFe hydrogels-based strain sensor exhibited a favorable GF of 1.23 even with a low doping concentration of ions.

In addition, the sensing performance of GPPFe hydrogel incorporated with different concentrations of $FeCl_3$ was also investigated (Figure S12). At low levels of $FeCl_3$ (0.07 M), the limited ion mobility in hydrogel resulted in low conductivity and corresponding reduced strain sensitivity (GF = 0.79). When the concentration of $FeCl_3$ increased to 0.33 M, although a larger number of ions can contribute to the enhanced conductivity (5.70 mS cm^{-1}), the change in sensing sensitivity is not obvious (GF = 1.22), indicating that the positive effect of concentration increase on GF value only occurs within a certain range. After exceeding a certain limit, excessive ions have insignificant effect on GF value. Therefore, the optimal concentration was determined to be 0.2 M due to the opportune balance where ultralow modulus ensures tissue conformality and high conductivity maintains sensing sensitivity.

In the practical application, different sensing applications require diverse suitable characteristics of sensing materials. The $GPPFe_{0.2\ M}$ hydrogel shows good flexibility, satisfying resilience, and adhesivity, which can be used to fabricate the strain sensor for the monitoring of human movement (Fig. 5a). As shown in Fig. 5b–d, we firstly attached the sensor on the finger joints of volunteers and recorded the changes of resistance with different angles (30° ~ 90°) of fingers. When the volunteers bent their fingers, deformation of hydrogels happened, and the resistance value of conductive hydrogel would change consequently. It can be observed that the wearable strain sensor based on $GPPFe_{0.2\ M}$ hydrogel exhibited significant response to the movement of fingers, and the change of resistance values increased with the bend

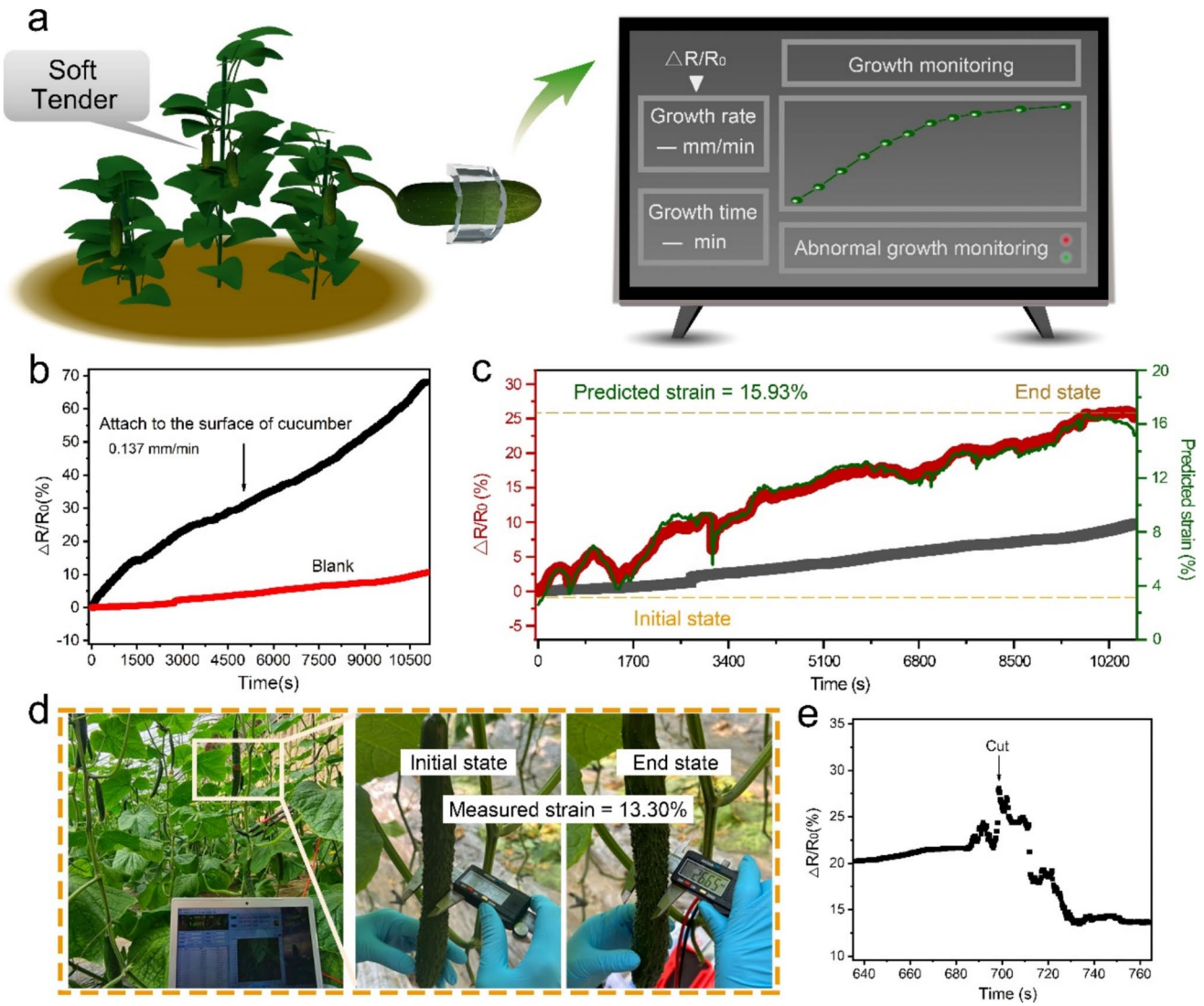

Fig. 6 **a** Application in plant growth monitoring of the $GPPFe_{0.2\ M}$ hydrogel. **b** Real-time monitoring of fruit growth rate during cucumber fruit growing. **c** Real-time monitoring of fruit growth and corresponding predicted strain value. **d** Real-world scene pictures collected during plant growth monitoring and the actual measured strain change. **e** Real-time resistance changes collected with the monitored cucumber fruit to be cut

angles of fingers increasing from 30° to 90°, indicating the good feasibility of the as-prepared strain sensor for the monitoring of human subtle actions. Then we attached the sensor on the wrist joints of volunteers and monitored the resistance value under different bending angles (30°~90°). As shown in Fig. 5e–g, the relative resistance variation increased with increasing the bending angle regularly, and the sensing signal can also reflect the bending speed, which can also be verified in the real-time resistance changes with the bending of elbow joints in Fig. 5 h. In addition, we also collected the sensing signal of the motion of knee joints (Fig. 5i–j). It can be observed that with the bending angle gradually increasing, the relative resistance variation increased correspondingly, while the curves were repeatable and regular at the same bending angle, demonstrating the satisfying reliability of GPPFe hydrogel to be used as a flexible wearable sensor in monitoring various human activities.

For the measurement of plant growth, especially the growth rate, low toughness and favorable stretchability were the crucial factors of conductive hydrogel considering that the plant tissue is delicate and susceptible to compression damage. When increasing the content of Fe^{3+} in G-PAAM/PVA IPN hydrogel to 0.2 M, the toughness and Young's modulus of hydrogel declined significantly, which enables suitable characteristics for the monitoring of growth rate and abnormal growth of plant fruits (Fig. 6a). Besides, in practical application, most of the hydrogels inevitably suffer from the evaporation of water in an open environment. To

avoid the severe dehydration of hydrogels in the long-term monitoring of plants growth, we introduced glycerol and $FeCl_3$ into PAAM/PVA double network hydrogel. Organic solvents like ethylene glycol and glycerol can inhibit water evaporation through interaction with water via strong hydrogen bonding, while inorganic salts can convert free water in hydrogels to bound water through the formation of hydrated ions and thereby increase the water retention ability of hydrogels. Therefore, GPPFe hydrogels exhibited significantly improved water retention ability, as shown in Figure S13. In addition, the effect of UV irradiation is a critical concern for the sensing stability of GPPFe hydrogels in real-world environments. We tested the strain sensing performance of the $GPPFe_{0.2\ M}$ hydrogel before and after different UV exposure times at 254 and 365 nm. As shown in Figure S14, $GPPFe_{0.2\ M}$ hydrogel exhibited a signal retention rate exceeding 97%, indicating stable strain sensing performance in UV exposure testing. The mechanical properties of $GPPFe_{0.2\ M}$ hydrogel were also measured before and after UV exposure (Figure S15). We observed that UV exposure at 254 and 365 nm altered the mechanical properties of the hydrogels, manifested by the increase in tensile strength after 36 h of irradiation, which indicated good stability against UV degradation.

Then we explored the possibility of $GPPFe_{0.2\ M}$ hydrogel to be applied in dynamically detecting the rate of fruit growth of plants (Fig. 6). The plant monitoring is conducted in a controlled greenhouse where ground irrigation eliminates direct water contact and stable microclimate conditions (75 ~ 80% RH at 25 ℃) ensure the stability of the hydrogel. In practical detection, the growing rate of plant fruits can be well reflected by the increased dimension of the fruits, which will also induce the variation of electrical resistance. Thus, the value of relative resistance change ($\Delta R/R_0$) can be referred to evaluate the growth of monitored plants. The sensor based on $GPPFe_{0.2\ M}$ conductive hydrogel was attached on the middle section of a cucumber to monitor the growing rate of fruits. On account of the gradually increased strain caused by the constant growing of fruits, the values of $\Delta R/R_0$ rose correspondingly, and the growing rate was calculated to be 0.137 mm/min accordingly (Fig. 6b). In addition, this sensor can also be applied for the monitoring of fruit size and provide the real-time predicted strain value as reference during the cultivation process (Fig. 6c). As shown in Fig. 6d, we measured the diameter size of the same section on cucumber fruit at the initial stage and final stage, and the predicted strain value (15.93%) was close to the actual measured value (13.3%), indicating the good feasibility of GPPFe hydrogel in plant growth monitoring. Besides, the potential of GPPFe hydrogel to be applied for the monitoring of abnormal growth was also investigated (Fig. 6e). Once the fruit was cut, the sensing signal declined promptly, which proved the potential of $GPPFe_{0.2\ M}$ conductive hydrogel to be used for monitoring the abnormal growth of plant fruits.

To investigate the toxicity of hydrogels, the cytotoxicity of the hydrogel was measured using NIH-3T3 cells by an MTT cytotoxicity assay. As shown in Figure S16, the cell viabilities were both > 70% after being cultured in extracts of GPPFe for 12 h while that of G-PAAM/PVA IPN hydrogel was about 98%, which can be ascribed to the inevitable cytotoxicity of residual monomer caused by incomplete polymerization. Thus, we must carefully consider the potential risk to directly attach the GPPFe hydrogels on human skin or the surface of plants in the practical application. One of the feasible strategies is to design an insulating underlayer with similar low Young's modulus, which can act as a buffer layer between the sensing layer and human body or plant fruits without compression injury. In addition, our current application scope for plant monitoring is exclusively confined to controlled greenhouses. To further expand the application scenarios to outdoor open-air environments, ion leaching risk under prolonged rainwater exposure should be considered. Meanwhile, long-term UV stability and water-retaining capacity of hydrogel remain a challenge. Encapsulating the GPPFe hydrogel would ensure sustainable plant monitoring in variable environments. Therefore, the design of a biocompatible buffer layer with appropriate mechanical properties is the focus of our future work.

3 Conclusion

In this work, to develop a wearable strain sensor based on ionic conductive hydrogels with required mechanical properties and tensile deformation capabilities for multipurpose biosensing, we prepared an ultrasoft and durable IPN hydrogel of GPPFe via ion pre-incorporation strategy. The amount and order of added Fe^{3+} strongly affect the formation of the two sub-networks of the IPN hydrogels, which in turn can regulate the mechanical toughness and flexibility of the hydrogels. On account of the improved flexibility and stretch deformation ability, $GPPFe_{0.2\ M}$ hydrogel exhibited increased adaptability for the monitoring of biological activities like human motion and plant growth considering its good conformal contact with biological surfaces and less pressure on the biological tissues. This work provided an innovative and simple strategy that can be generalized to the fabrication of various ultrasoft ionic conductive hydrogels based on synthetic hydrogels for the practical wearable electronics devices.

4 Experimental procedures

4.1 Reagents and chemicals

Polyvinyl alcohol (PVA), poly(acrylamide) (PAAM), ammonium persulfate (APS), N,N'-methylenebisacrylamide (MBAA), iron (III) chloride hexahydrate, and glycerol were purchased from Shanghai Macklin Biochemical Co. Ltd. All chemicals were of analytical grade and used without further purification. Deionized water was utilized to prepare aqueous solutions in the experiment.

4.2 Preparation of conductive hydrogels

To prepare the GPPFe hydrogel, 0.003 g of MBAA, 3 g of PVA, and 3 g of PAAM powder were dissolved in 20 mL of deionized water at 90 ℃ for 5 h to obtain a homogeneous solution. Subsequently, 5 mL of glycerol was introduced, and the solution was heated at 90℃ for 10 min after mixing. Then the above-mentioned solution was supplemented with 1.5 mL of $FeCl_3$ solution and heated at 90 ℃ for 10 min. After the mixture was allowed to cool naturally to room temperature, 1.5 mL of 2.2 M APS was added under stirring. Based on the final $FeCl_3$ concentrations in the system (0.07 M, 0.15 M, 0.2 M, 0.26 M, or 0.33 M), the hydrogels were named $GPPFe_{0.07\ M}$, $GPPFe_{0.15\ M}$, $GPPFe_{0.2\ M}$, $GPPFe_{0.26\ M}$, and $GPPFe_{0.33\ M}$, respectively. The resulting mixture was poured into a clean plastic plate and polymerized at 60 °C for 10 h; then the GPPFe hydrogel was obtained after three freeze–thaw cycles executed in a refrigerator (− 20 ℃) and at room temperature.

For comparison, the IPN hydrogel of G-PAAM/PVA and SN hydrogel of PVA were also prepared. For the preparation of the IPN hydrogel of G-PAAM/PVA, the procedure is the same as the above method but without the addition of $FeCl_3$. For the preparation of the SN hydrogel of PVA, 3 g of PVA was dissolved in 20 mL of deionized water at 90℃ for 5 h to obtain a homogeneous solution; then, 5 mL of glycerol was introduced, and the solution was heated at 90℃ for 10 min after mixing. The mixture was allowed to cool naturally to room temperature; the PVA SNs were obtained after three freeze–thaw cycles. For the preparation of the G-PAAM/PVA IPN hydrogel with post-incorporated Fe^{3+} ($GPPFe_{0.2\ M\ post}$), the G-PAAM/PVA IPN hydrogel was immersed in 0.2 M $FeCl_3$ solution for 10 h, and then it was transferred into deionized water and immersed for 5 h to remove the superfluous ions. The hydrogel with post-incorporated Fe^{3+} stabilized at room temperature for 24 h to obtain $GPPFe_{0.2\ M\ post}$ hydrogel.

4.3 Characterization

To observe the surface microstructures of prepared hydrogels, field-emission scanning electron microscopy (SEM, S-4800, Hitachi, Japan) was used. The surface chemical composition of prepared hydrogels was analyzed by ESCALAB MKII X-ray photoelectron spectrometer. Fourier transform infrared (FT-IR, Nicolet 8700, USA) spectroscopy was utilized to investigate the chemical structure of the hydrogels. The mechanical properties of prepared hydrogels were measured by a texture analyzer (TA.XT PLUS/50, STABLEMICVO, Britain) at room temperature. To carry out the rheological measurement, a rheometer (DHR-1, Waters, USA) was utilized with a parallel plate (diameter 20 mm). Thermal gravimetric analysis (TGA) of the hydrogels was measured by a thermal analyzer (TGA/DSC 3 +, Mettler Toledo, Switzerland). X-ray diffraction (XRD) patterns were obtained using a Bruker D8 Advance diffractometer (Rigaku, Japan).

4.4 Electrical tests

To determine the conductivities of prepared hydrogels, the electrochemical impedance spectroscopy (EIS) curves were measured on a CHI660E electrochemical workstation (CH Instruments, China) with two copper plates used as electrodes. A digital multimeter (Victor 8246 A, Victory Instruments Co. Ltd., China) connected to a computer was implemented to detect the sensing performance of the hydrogel sensors.

4.5 Biocompatibility test

NIH3T3 cells were cultured in a DMEM medium containing 10% FBS and 1% double antibody. Cells were incubated in an incubator at 37 °C and 5% CO_2. The cells were seeded into a 96-well plate and incubated for 12 h; then the mixture of complete medium and extract of GPPFe hydrogel was added into each 96-well plate. After being incubated for 12 h, the cells were treated with MTT solution. After culturing for 4 h, we removed the supernatant and added dimethyl sulfoxide (DMSO, 100 μL) into each 96-well plate to dissolve blue-purple formazan. Finally, the cell viability was calculated by measuring the absorbance of each 96-well plate at 495 nm using a microplate reader (Tecan Austria GmbH, Salzburg, Austria).

Supplementary Information The online version contains supplementary material available at https://doi.org/10.1007/s42114-025-01422-x.

Acknowledgements We appreciate the kind support from the National Key Research and Development Program of China (No. 2023YFE0103300), the Natural Science Foundation of China (22102133), the Innovative Talent Promotion Program-Science & Technology Innovation Team of Shaanxi (No. 2023-CX-TD-55), Qinchuangyuan"Scientist + Engineer"team of Shaanxi (2022KXJ-070), Qinghai Special Project of Innovation Platform for Basic Conditions of Scientific Research of China (2022-ZJ-Y18) and the Key Research and Development Program of Shaanxi Province (No. 2022NY-13). We thank the State Key Laboratory of Crop Stress Biology for Arid Areas, Northwest A&F Universiy (Guoyun Zhang) for technical support in SEM analysis.

Author contribution Yiyue Ma conceived the concept, designed the experiments, conducted the tests and data analysis, and wrote the manuscript. Congdi Shang provided guidance on data analysis, and contributed to the writing and review process. Yiting Xu and Xintong Wu supported the data collection. Wenxin Zhu supervised the research and provided overall guidance. Wenzhi Tang, Hai Tan and Jianglong Wang assisted in providing facilities and scientific discussion as well as supervised the project.

Funding We appreciate the kind support from the National Key Research and Development Program of China (No. 2023YFE0103300), the Natural Science Foundation of China (22102133), the Innovative Talent Promotion Program–Science & Technology Innovation Team of Shaanxi (No. 2023-CX-TD-55), Qinchuangyuan"Scientist + Engineer"team of Shaanxi (2022KXJ-070), Qinghai Special Project of Innovation Platform for Basic Conditions of Scientific Research of China (2022-ZJ-Y18), and the Key Research and Development Program of Shaanxi Province (No. 2022NY-13).

Data availability No datasets were generated or analysed during the current study.

Declarations

Conflict of interest The authors declare no competing interests.

References

1. Chai Y, Chen C, Luo X, Zhan S, Kim J, Luo J, Wang X, Hu Z, Ying Y, Liu X (2021) Cohabiting plant-wearable sensor in situ monitors water transport in plant. Adv Sci 8(10):2003642
2. Tang W, Yan T, Ping J, Wu J, Ying Y (2017) Rapid fabrication of flexible and stretchable strain sensor by chitosan-based water ink for plants growth monitoring. Adv Mater Technol 2(7):1700021
3. Lee S, Franklin S, Hassani FA, Yokota T, Nayeem MO, Wang Y, Leib R, Cheng G, Franklin DW, Someya T (2020) Nanomesh pressure sensor for monitoring finger manipulation without sensory interference. Science 370:966–970
4. Hu L, Chee PL, Sugiarto S, Yu Y, Shi C, Yan R, Yao Z, Shi X, Zhi J, Kai D, Yu HD, Huang W (2023) Hydrogel-based flexible electronics. Adv Mater 35(14):e2205326
5. Sheng F, Yi J, Shen S, Cheng R, Ning C, Ma L, Peng X, Deng W, Dong K, Wang ZL (2021) Self-powered smart arm training band sensor based on extremely stretchable hydrogel conductors. ACS Appl Mater Interfaces 13(37):44868–44877
6. Ma C, Ma MG, Si C, Ji XX, Wan P (2021) Flexible MXene-based composites for wearable devices. Adv Func Mater 31:2009524
7. Dragan ES (2014) Design and applications of interpenetrating polymer network hydrogels. A review. Chem Eng J 243:572–590
8. Wang L, Xu T, Zhang X (2021) Multifunctional conductive hydrogel-based flexible wearable sensors. TrAC Trends Anal Chem 134:116130
9. Zheng H, Lin N, He Y, Zuo B (2021) Self-healing, self-adhesive silk fibroin conductive hydrogel as a flexible strain sensor. ACS Appl Mater Interfaces 13(33):40013–40031
10. Liu Y, Huang J, Li S, Li Z, Chen C, Qu G, Chen K, Teng Y, Ma R, Wu X, Ren J (2024) Advancements in hydrogel-based drug delivery systems for the treatment of inflammatory bowel disease: a review. Biomater Sci 12(4):837–862
11. Shan B-H, Wu F-G (2024) Hydrogel-based growth factor delivery platforms: strategies and recent advances. Adv Mater 36(5):2210707
12. Guo S-J, Chang H-Y, Xu M-J, Wang C-X, Wei H, Li D-D, Chen J, Zhou Y, Liu Y (2022) Co2+-mediated hydrogels with enhanced mechanical properties for flexible sensing. ACS Appl Polym Mater 4(9):6403–6413
13. Fang L, Hu J, Zhang CW, Wei J, Yu HC, Zheng SY, Wu ZL, Zheng Q (2022) Facile synthesis of tough metallosupramolecular hydrogels by using phosphates as temporary ligands of ferric ions to avoid inhibition of polymerization. J Polym Sci 60(15):2280–2288
14. Mastrangelo R, Chelazzi D, Poggi G, Fratini E, Pensabene Buemi L, Petruzzellis ML, Baglioni P (2020) Twin-chain polymer hydrogels based on poly(vinyl alcohol) as new advanced tool for the cleaning of modern and contemporary art. Proc Natl Acad Sci U S A 117(13):7011–7020
15. Zhang T, Hu X, Zu B, Dou X (2022) Bilayer hydrogel sensor boosted ng-level solid nitrite detection through asymmetrical diffusion construction facilitated colorimetric signal enhancement. Sens Actuators B: Chem 369:132324
16. Wang X, Wang B, Cheng J (2023) Multi-healable, mechanically durable double cross-linked polyacrylamide electrolyte incorporating hydrophobic interactions for dendrite-free flexible zinc-ion batteries. Adv Funct Mater 33(43):2304470
17. Das P, Ganguly S, Marvi PK, Hassan S, Sherazee M, Mahana M, Tang X, Srinivasan S, Rajabzadeh AR (2025) Silicene-based quantum dots nanocomposite coated functional UV protected textiles with antibacterial and antioxidant properties: a versatile solution for healthcare and everyday protection. Adv Healthc Mater 14(6):2404911
18. Min Jinbiao, ZZ, Zheng Jia, Yan Caibin, Sha Hongyuan, Hong Maochun, Fu Heqing (2022) Self-healing, water-retaining, antifreeze, conductive PVA/PAA-PAM-IS/GC composite hydrogels for strain and temperature sensors. Macromol Mater Eng 307:2100948
19. Sekkal M, Dincq D, Legrand P, Huvenneb JP (1995) Investigation of the glycosidic linkages in several oligosaccharides using FT-IR and FT Raman spectroscopies. J Mol Struc 349:349–352
20. Waly AL, Abdelghany AM, Tarabiah AE (2021) Study the structure of selenium modified polyethylene oxide/polyvinyl alcohol (PEO/PVA) polymer blend. J Mater Res Technol 14:2962–2969
21. Unsalan O, Szolnoki B, Toldy A, Marosi G (2012) FT-IR spectral, DFT studies and detailed vibrational assignment on N, N', N''-tris(2-aminoethyl)-phosphoric acid triamide. Spectrochim Acta A Mol Biomol Spectrosc 98:110–115
22. Unsalan O, Szolnoki B, Toldy A, Marosi G (2012) FT-IR spectral, DFT studies and detailed vibrational assignment on N,N', N"-tris(2-aminoethyl)-phosphoric acid triamide. Spectrochim Acta A Mol Biomol Spectrosc 98:110–115
23. Cao Z, Zheng X, Huang W, Wang Y, Qu Q, Huang Y, Zheng H (2021) Molecular design of a multifunctional binder via grafting

and crosslinking for high performance silicon anodes. J Mater Chem A 9(13):8416–8424
24. Ganguly S, Wulff D, Phan C-M, Jones LW, Tang XS (2024) Injectable and 3D extrusion printable hydrophilic silicone-based hydrogels for controlled ocular delivery of ophthalmic drugs. ACS Appl Bio Mater 7(9):6286–6296
25. Cheng-Fei Li L-JX (2022) Jia-Wei Zhao, Lin-Fei Gu, Hai-Bo Tang, Lirong Zheng, and Gao-Ren Li, Interfacial Fe O Ni O Fe bonding regulates the active Ni sites of Ni-MOFs via iron doping and decorating with FeOOH for super-efficient oxygen evolution. Angew Chem Int Ed 61:202116934
26. Choi HW, Woo HJ, Hong W, Kim JK, Lee SK, Eum CH (2001) Structural modi®cation of poly(methyl methacrylate) by proton irradiation. Appl Surf Sci 169–170:433–437
27. Jin X, Sun G, Zhang G, Yang H, Xiao Y, Gao J, Zhang Z, Qu L (2019) A cross-linked polyacrylamide electrolyte with high ionic conductivity for compressible supercapacitors with wide temperature tolerance. Nano Res 12(5):1199–1206
28. Min Jinbiao, ZZ, Zheng Jia, Yan Caibin, Sha Hongyuan, Hong Maochun, Fu Heqing (2022) Self-healing, water-retaining, antifreeze, conductive PVA/PAA-PAM-IS/GC composite hydrogels for strain and temperature sensors. Macromol Mater Eng 307:2100948
29. Jorly Joseph EDJ (2007) Red-, blue-, or no-shift in hydrogen bonds: a unified explanation. J Am Chem Soc 129:4620–4632
30. Li Z, Yang H, Li P, Liu J, Wang J, Xu Y (2013) Fruit biomechanics based on anatomy: a review. Int Agrophys 27(1):97–106
31. Li Z, Wang Y (2016) A multiscale finite element model for mechanical response of tomato fruits. Postharvest Biol Technol 121:19–26
32. Li M, Pan G, Zhang H, Guo B (2022) Hydrogel adhesives for generalized wound treatment: design and applications. J Polym Sci 60(8):1328–1359
33. Tang W, Yan T, Wang F, Yang J, Wu J, Wang J, Yue T, Li Z (2019) Rapid fabrication of wearable carbon nanotube/graphite strain sensor for real-time monitoring of plant growth. Carbon 147:295–302
34. Watanabe M, Kiuchi H (1962) Effects of cupric salts on the polymerization of acrylonitrile in aqueous solution. J Polym Sci 58(166):103–119
35. Wu Y, Prulho R, Brigante M, Dong W, Hanna K, Mailhot G (2017) Activation of persulfate by Fe(III) species: implications for 4-tert-butylphenol degradation. J Hazard Mater 322:380–386
36. Li G, Zhang Y, Zhang X, Zhang J, Sun B (2024) Deciphering the formation of Fe(IV) in the Fe(II)/peroxydisulfate process: the critical role of sulfate radical. Environ Sci Technol 58(35):15864–15873
37. Chen Y, Li Y, Wang Y, Zhang IY, Huang R (2023) Efficient removal of recalcitrant naphthenic acids with electro-cocatalytic activation of peroxymonosulfate by Fe(III)-nitrilotriacetic acid complex under neutral initial pH condition. J Hazard Mater. https://doi.org/10.1016/j.jhazmat.2023.131524
38. He H, Li H, Pu A, Li W, Ban K, Xu L (2023) Hybrid assembly ofpolymeric nanofiber network for robust and electronically conductive hydrogels. Nat Commun 14:759
39. Lei T, Wang Y, Zhang Q, Wang H, Duan X, Yan J, Xia Z, Wang R, Shou W, Li X, Fan J (2024) Ultra-stretchable and anti-freezing ionic conductive hydrogels as high performance strain sensors and flexible triboelectric nanogenerator in extreme environments. Nano Energy 126:109633
40. Pei Z, Ding L, Wang C, Meng Q, Yuan Z, Zhou Z, Zhao S, Chen Y (2021) Make it stereoscopic: interfacial design for fulltemperature adaptive flexible zinc–air batteries. Energy Environ Sci 14:4926
41. Das P, Ganguly S, Marvi PK, Sherazee M, Tang X, Srinivasan S, Rajabzadeh AR (2024) Carbon dots infused 3D printed cephalopod mimetic bactericidal and antioxidant hydrogel for uniaxial mechanofluorescent tactile sensor. Adv Mater 36(48):2409819
42. Xie H-Q, Xiang Q (2000) Surface-graft polymerization of doped polyaniline with hydrophilic monomers. Eur Polym J 36(3):509–517